INTERACTIONS OF 200 GeV PROTONS WITH EMULSION NUCLEI

INTERACTIONS OF 200 GeV PROTONS WITH EMULSION NUCLEI

by

Gerd F. Hartner

A thesis submitted to the Faculty of
Graduate Studies and Research in partial
fulfillment of the requirements for the
degree of Master of Science.

Department of Physics
McGill University
Montreal, Que.
Canada

August 1973

ABSTRACT

Interactions of 200 GeV Protons with Emulsion Nuclei

Gerd F. Hartner
Department of Physics

M.Sc. Thesis
McGill University

The measurement and analysis of inelastic collisions between 200 GeV protons and emulsion nuclei are presented. The inelastic mean free path obtained is 33.9 ± 2.3 cm. Average charged multiplicities of shower particles and nuclear fragments are $< N_s > = 13.1 \pm 0.3$ and $< N_h > = 7.8 \pm 0.2$, respectively. Angular and rapidity distributions of events with less than two charged nuclear fragments are obtained. These events include a small sample of possible coherent stars which have been separated by angular coherence criteria. A comparison of shower multiplicity and rapidity distribution results with models of coherent and incoherent intranuclear production is given.

RESUMÉ

Interactions protons-noyaux à 200 GeV dans les émulsions nucléaires

Gerd F. Hartner
Département de Physique

Thèse de Maîtrise
Université McGill

Nous présentons la mesure et l'analyse des collisions inélastiques de protons de 200 GeV sur les noyaux de l'émulsion. Le libre parcours moyen pour ces collisions inélastiques est de 33.9 ± 2.3 cm. La multiplicité chargée des particules produites est: $< N_s > = 13.1 \pm 0.3$ et celles des fragments nucléaires est: $< N_h > = 7.8 \pm 0.2$. Nous donnons la distribution angulaire et la rapidité pour les événements ayant moins de deux fragments chargés. Cet échantillon comprend des candidats à la production cohérente que nous avons séparés par des critères angulaires de cohérence. Les résultats obtenus pour la multiplicité des particules chargées et la rapidité sont comparés aux modèles de production intranucléaire cohérente et incohérente.

PREFACE

This thesis contains work that has been done since August 1972 on the study of inelastic interactions of 200 GeV protons with complex nuclei. I would like to express my gratitude to Professor P. M. Patel for providing a great amount of constant guidance and sound advice, as well as the opportunity to explore this field. My understanding of physical processes involved has also benefitted from discussions with Professor B. Margolis and Dr. W. J. Meggs of the McGill Physics Department, and Mr. H. Areti of the University of Ottawa.

I wish to thank Dr. Suzanne Vallet of the University of Quebec at Montreal for kindly translating the abstract, Miss Katheleen Gardiner and Mr. Paul Brockman for carrying out some of the data reduction, and Miss Beverly Abbey who, despite my many revisions, patiently typed the manuscript.

It is a special pleasure to acknowledge the help of Professors Jacques and Joan Hébert who skilfully developed the emulsions and allowed me access to the facilities of their Nuclear Emulsion Laboratory at the University of Ottawa. Their guidance and training in the initial stages was invaluable.

TABLE OF CONTENTS

1. INTRODUCTION

We describe the measurement and analysis of inelastic collisions between 200 GeV protons and emulsion nuclei. The technique of nuclear emulsions is one of the oldest tools of high energy physics [see reference (1) for further references relevant to this discussion]. Nuclear emulsions allow excellent "spatial correlation", but no "time correlation", of the event. They provide many ways of detecting nuclear excitation or nuclear break-up, such as emission of evaporation prongs or of electrons due to internal conversion. Unfortunately, the nature of the target nucleus is usually unknown and tremendous scanning effort is required to obtain reasonable statistics. However, emulsions are extremely useful for pioneering work at large accelerators or with cosmic rays, due to their limited size and weight, low cost and simplicity of installation. In fact, at most accelerators they provided the first glimpse of the behavior in complex nuclei of the highest energy particles available.

Work was done at McGill University as part of an international collaboration whose members are listed in reference 2. Results include inelastic mean free path, charged nuclear fragment multiplicity distribution, charged shower particle multiplicity distribution, and a comparison to models of coherent and incoherent intranuclear production. Our results also include charged shower particle angular distributions for various categories of events containing no more than one heavy track due to nuclear fragments. We were not able to measure angular distributions for stars of all sizes for two reasons. First, the emulsion plate, which was vertically exposed to the proton beam, was too thin to allow observation of some shower particles in regions where vision was not optically distorted by the presence of many heavily ionizing nuclear fragments produced in the collision. Secondly, the thinness of the plate, together with development distortions and visual resolution limitations, did not permit an accurate measurement of small angles ($< 0.2^{\circ}$). Thus, it was necessary to supplement our results with distributions for large events obtained by other members of the group who used longitudinally exposed plates in which the difficulties mentioned above are not present. These distributions appear in Section 5.5 with other preliminary results of our collaboration(2,3) for the purposes of comparison to and extension of our own data. Apart from this, all the work here was done at McGill.

2. EXPERIMENTAL DETAILS

2.1 Exposure to Beam

Three stacks of Ilford K5 emulsion were exposed to the NAL 200 GeV proton beam in September, 1972. The exposure took place in the NAL Meson Target Area, displayed in Figure 1. The beam used had a final cross-sectional area of 3cm x 8cm and a flux of ∿ 10^4 protons/pulse. Defocusing of the beam (from its ∿ 1mm diameter spot) was done in the proton beam transport system so that at the entrance to the Meson Target Hall it had the aperture mentioned above. This was done to avoid any excessive scraping by the pole pieces in the last bending magnet situated at the beginning of the target area. From here to the target box, which was the approximate location of the emulsions, the beam travelled through a helium gas bag. The total path length in the helium gas bag was ∿ 100 ft. Beam spot alignment was done with polaroid film and checked with an emulsion test plate. Relative beam monitoring was provided by a scintillation counter telescope situated just behind the emulsion, and was calibrated using the emulsion test plate. For reliable calibration during actual exposure an amount of material (∿ $2 gm/cm^2$) equivalent to the emulsion stack was inserted in the beam path. Any contamination from secondary particles produced by the primary proton beam in He or other material encountered by the beam before hitting the emulsion stack was reduced to a minimum by a) only scanning in the middle of the beam cross-sectional area, and b) enforcing rigid criteria on beam particle parallelism ($<$ 3 milliradians).

2.2 Emulsion Stack Development

Two stacks of emulsion (40 pellicles each), having approximate dimensions 20cm x 5cm x 600μ, were exposed horizontally (beam parallel to the emulsion surface) to a flux of 2 x 10^4 protons/cm^2. The third stack (20 pellicles), having dimensions

5cm x 5cm x 600µ was exposed vertically (beam perpendicular to the emulsion surface) to a flux of about 10^6 protons/cm^2. The density of the emulsion at the time of exposure was 3.75 gm/cm^3. Processing of the two horizontal stacks was carried out in Strasbourg while the smaller vertical stack was processed in Ottawa. In each case a two-temperature development technique, using a dry hot-stage was employed.

2.3 Composition and Description of Emulsion Plate

The plate consists of a pellicle labelled V8 from the vertically exposed stack mounted on a glass backing. At the time of exposure to the beam the pellicle was 646 µ thick and had a density of 3.75 gm/cm^3. Using as reference(4) the known composition of Ilford K5 emulsion at 58% relative humidity and density 3.828 gm/cm^3, the water content was calculated. Atomic densities and quantities such as mean atomic number and charge appear in Table 1.

During processing at Ottawa a grid of coordinates was printed on the surface of the pellicle adjacent to the glass backing. The grid consists of squares of side .5mm in which are inscribed two sets of numbers identifying an XY-plane. Development processes caused the emulsion to shrink to a thickness of 274-282 µ. Thickness variations depend primarily on humidity changes which cause emulsion gelatin to shrink or swell. Flux was found to vary between 7.3 x 10^5 and 1.1 x 10^6 protons/cm^2 in the regions scanned, however the variations were negligible in square areas of side 1mm.

Under the microscope beam protons appear as a lattice of dots, each of which ~~is~~ ∿ 0.5 µ diameter. As one traverses the depth of emulsion, from the top where the beam enters down to the grid where it leaves, the lattice is displaced in the XY-plane by 5 to 15 µ. This shift is due to development distortions and imperfect alignment of emulsion stack with respect to beam.

3. METHOD OF SCANNING

3.1 Equipment

The indispensible instrument for emulsion measurements is the microscope, in our case an old Leitz Wetzlar used by Dr. John Foster which we subsequently overhauled. The microscope is equipped with adjustable binocular tube, revolving turret mount capable of holding four objectives, object stage with 8cm. and 5 cm. scales in the X and Y directions respectively, and built-in Kohler illuminating system. Light is generated by a variable power supply. Microscope and power supply specifications are given in Table 2.

Table 3 describes the optics used for various purposes in terms of working distance, numerical aperture (N.A.), resolution, and depth of focus (Δ)(4). Working distance refers to displacement between tip of objective and point of focus. Resolution, determined by the numerical aperture and the wave length in air of light used, is approximately given by $.5\lambda/$N.A.. Numerical aperture is $n \sin \alpha$ where n is the index of refraction and α the extreme ray to the axis. Depth of focus is the interval along the axis of the objective over which the sharpness of the visual image does not noticeably change, and determines the accuracy with which the depth of an event may be measured. Δ is given by $\lambda/(4n \sin^2 \alpha/2)$, where α is determined from the definition of N.A.. Air objectives give crisp pictures but have small numerical apertures and cause grave geometrical distortions at high power since index of refraction changes occur at air-lens and air-emulsion boundaries. Immersion oil objectives greatly reduce this problem because lens glass, immersion oil, and emulsion gelatin all have $n \sim 1.5$.

Of course other microscope accessories were necessary. Immersion oil, in addition to its obvious purpose, also serves to disperse heat absorbed in the emulsion from the illuminating light. This helps to prevent the emulsion which is composed mainly of organic constituents from being damaged at the focal point. We used green filters to make the image pleasant and reduce the width of the light frequency spectrum used. Reticles placed in the oculars served to superimpose scales, reference axes, or coordinate grids on the image plane. Reticle patterns were calibrated using a stage micrometer consisting of a 1 mm. rule with 100 ten μ divisions. We designed the emulsion room and equipped it with a hygrometer-thermometer, humidifier, dehumidifier, and air conditioner. Temperature is maintained at ∿ 72° ± 3 and relative humidity at ∿ 55 ±5%. Prolonged exposure to overly damp air makes emulsion swell, soften and fog, while dry air makes it shrink, causing stresses capable of peeling the emulsion from the glass plate.

From this description it is clear that all information was obtained from manual scanning. Development of automatic scanning techniques for emulsion physics is very slow due to the serious problems mentioned above, and because of the complicated appearance of many interactions in nuclei. This is unfortunate since finding and analyzing an event usually requires several hours of eye-straining tedious labor.

3.2 Technique

3.2.1 Assessment of Vertical Beam Exposure Method

Vertical (or transverse) beam exposure results in several advantages over longitudinal (or parallel) exposure. The beam flux may be chosen two orders of magnitude greater because paths appear as an almost continuous sequence of dots, each of which is reinforced by the shadows of its nearest neighbors above and below. Using the Z-motion microscope control such paths are much easier and more rapidly followed than the side view as seen in parallel plates, where only about twenty grains are developed and statistically scattered along one hundred microns of track length. Another advantage is the shrinkage of emulsion during development by more than a factor of two. This means more track is scanned than indicated by the Z-motion micrometer, and results also in larger and therefore more easily measured shower particle angles. With the optics we used some $10^5\mu$ of beam track were followed in each field view. With the same optics only about 200μ of path length could be followed on a parallel plate before a change of field became necessary in the along-the-track scanning technique.

However, vertical area scanning has a serious disadvantage compared to parallel track scanning. The problem is that events with small showers and few or no nuclear fragments are so much harder to see than events with nuclear disintegrations. Since 75% of all events are these easily seen incoherent events the scanner is likely to scan too quickly to see the smaller events with reasonable efficiencies. The problem is not encountered by along-the-track scanners who recognize any interaction when the track they follow becomes a set of tracks, or at least changes direction.

3.2.2 Procedure for Event Scanning

An area of 1 mm^2 is chosen, defined by four neighbouring .5 mm square coordinate grids. Flux is counted near the center of this area and is used to represent the whole region. This flux counting is done by means of a reticle inscribed with a 10 square by 10 square grid whose image dimensions are obtained using the stage micrometer. To be counted as a beam proton a track is followed from the surface for about 100 μ of Z-motion to ensure that it is parallel to the lattice formed by other beam tracks.

The same reticle is used for event scanning. A group of several protons is observed during one or more traverses between top and bottom of the plate. If a beam track is seen to develop into a shower the scanner records the depth of the event, the projected position on the emulsion coordinate grid, and makes a rough count of the number of heavily ionizing and minimum ionizing tracks. This information defines the appearance and position of the event so that it may be later revisited for further analysis. The scanner then proceeds to observe a new group of protons and eventually covers the area seen within the reticle grid. Using the X and Y motion controls, an adjacent field of view is chosen and the process repeated, until the entire mm^2 is scanned. An example of how we recorded scanning data for a typical mm^2 is shown in Figure 2.

3.2.3 Procedure for Track Classification

Tracks are classified according to grain density g. If the beam protons have a grain density g_o ($\sim$ 17 grains developed /100μ) then the classifications are:

black	$g_b > 4\,g_o$
grey	$4g_o > g_g > 1.4g_o$
minimum	$1.4g_o > g_m$

Minimum tracks are formed by singly charged relativistic particles, and are attributed to beam tracks and shower particle tracks. Black and grey tracks are formed by non-relativistic singly or multiply charged particles, and are attributed to nuclear fragments although there is a small contamination by slow pions (discussed in Section 5.5). These fragments are produced when the nucleus rearranges itself after the incident proton punched a hole through it. Black tracks less than 5μ in length are caused by nuclear recoils. In emulsion one can observe fairly slow(5) recoils ($\sim$ 0.2 MeV protons and $\sim$ 1 MeV carbon nuclei).

Tracks are classified for each event by counting the number of black tracks N_b, the number of grey tracks N_g, the number of minimum tracks N_s, and by noting if a recoil is visible. The total number of charged fragments is called $N_h = N_b + N_g$. Occasionally a track can not be followed for distances long enough to establish its category. If a choice between black or grey must be made then there is no problem because in any case the particle will be considered to be a nuclear fragment. If a choice between grey or minimum could not be resolved, the scanner made a best estimate based on the limited information available. Fortunately, a determination by grain counting can usually be made before this stage is reached.

Figure 3 shows how track classification data was recorded. If the event was too low in the emulsion to allow a definite shower count then it was passed over for the next event. Events are centered on a Cartesian coordinate axis reticle, and each octant is searched using the microscope Z-motion. "Forward Shower" refers to those minimum tracks at angles $\lesssim 10^\circ$ with respect to the beam direction. At these small angles minimum tracks are easy to see because they diverge slowly from the incident beam direction. Shower tracks at larger angles are more difficult to see because there are considerable gaps in the XY-plane (as well as the Z-direction) between developed grains. These "Transverse Shower" tracks may be seen by following imaginary lines outward from the interaction vertex while varying the Z-motion control at different rates. The track appears as a sequence of developed grains along one of these imaginary lines. Care must be taken to ensure that the sequence is not from a random background of developed grains. The tracks of electrons and positrons (e.g. from e^+e^- pairs or knock-on electrons) must also be discarded. These may be recognized by twisting tracks characteristic of large angle multiple Coulomb scattering of light mass particles.

3.2.4 Procedure for Angle Measurements

Let θ be the angle of a shower particle with respect to the beam direction. Let $\vec{B}$ be a vector defining the beam direction, and $\vec{S}$ a vector defining the direction of the shower particle. Then $\cos\theta = \vec{B}\cdot\vec{S}/(|\vec{B}|\cdot|\vec{S}|)$. Thus the angle is determined by a measurement of the vectors $\vec{B}$, $\vec{S}$.

Choice of a Z-value for these vectors is the result of a compromise between large values to better define a direction and small values to reduce the effects of development strains which are sometimes very serious near the emulsion bottom. Since these strains can never be completely avoided Z_B and Z_S are chosen between the same emulsion depths whenever possible so that both $\vec{B}$ and $\vec{S}$ may be distorted in the same way. Z_S is measured directly from the interaction vertex toward the emulsion bottom. However Z_B must be measured using a nearby beam particle, since the original is usually deflected during the collision. The values of Z obtained using the Z-motion micrometer must be multiplied by the shrinkage factor

$$S = \frac{\text{thickness of emulsion during exposure to beam}}{\text{thickness during measurement of Z}}$$

to obtain the actual displacement desired. Accuracy of Z measurements is determined by the ability to locate the exact position of the vertex and by the depth of focus Δ. The X and Y values are obtained by using a reticle scale calibrated with the stage micrometer. The particle is centered on the scale at the vertex depth, and its

X or Y value measured at a depth $Z\mu$ below. Accuracy of the X or Y measurements is determined by the scale calibration, by the optical resolution, and by the developed grain diameter. These quantities as well as optics are specified in Table 4.

Figure 4 shows a sample set of angle measurements. For each event the shower prongs are sketched and labelled to avoid confusion. Then components of $\vec{B}$ and each of the vectors $\vec{S}$ are obtained as described above. ΔZ_v, the uncertainty in vertex position, is estimated from noting the limiting depths at which the beam is definitely still above the collision, and at which the shower is definitely in existence. The angle θ and its deviation $\Delta\theta$ are calculated. Sin θ values for each shower particle are necessary for the application of a coherence criteria (see Section 4.5). The quantity $\log_{10} \tan \theta$ is related to the rapidity, and its expectation value can be used to determine the effective center of mass velocity (see Section 5.4). It is clear that errors are large for small θ, however, they are of a nature which is not expected to seriously affect the results obtained from these angle measurements. Section 5.4 contains a further discussion of these errors.

4. ANALYSIS OF DATA

4.1 Efficiency

We wish to demonstrate why efficiency corrections(6) were not very important for our work. Suppose a sample of emulsion containing N events is scanned by two observers A and B with efficiency factors η_A, η_B respectively. Let n_1 be the number of events which both observe, n_2 the number which A observes but not B, and n_3 the number which B observes but not A.

Then by definition:

$$n_1 = \eta_A \eta_B N$$

$$n_2 = \eta_A (1 - \eta_B) N$$

$$n_3 = \eta_B (1 - \eta_A) N$$

so that $$\eta_A = \frac{n_1}{n_1 + n_3} , \quad \eta_B = \frac{n_1}{n_1 + n_2}$$

and $$N \simeq \frac{(n_1 + n_2)(n_1 + n_3)}{n_1}$$

The method assumes events missed are purely random. However biases exist because both scanners will tend to miss difficult events. For instance, events (or stars) with $N_h \leq 1$ are much harder to see than stars with $N_h > 1$. Therefore, separate efficiencies must be defined for these categories. Furthermore, events with $N_h \leq 1$ and low N_s are much harder to see than other $N_h \leq 1$ events; more efficiency factors must be calculated.

Consider Table 5 which shows the results of a rescan of 11 mm^2 (out of 23 total scanned) at larger magnification and perhaps half the rate of the initial scan. Both scans, though performed by the author, were independent. Two details immediately evident are that all events seen in the first scan A were also seen in scan B, and that 70 % of the $N_h = 0$, $N_s \leq 7$ events seen in scan B were missed in scan A. Clearly a rescan of the region under the same circumstances as scan A would not be expected to be a reliable means of determining the true number of events in a given $N_h \neq 0$, low N_s category.

Furthermore, it became clear that we would not be able to amass good statistics at either scanning rate with our scanning power. This was based on the observation that finding an event, classifying its tracks, and doing angular shower measurements each required periods of the order of one hour at the microscope. We therefore concluded that a statistically small but accurate collection of events which could be combined with data from the line-scanning members of our collaboration was the only solution. This course dictated a method as in scan B. Since our results agree(to within statistics) with those of the parallel plate line scanners, we feel our method has been justified.

4.2 Estimate of 1-Prong White Stars

While scanning for inelastic interactions we did not unambiguously identify any clean (i.e. $N_h = 0$, no recoil) 1-prong events. It is easy to imagine that such events, characterized by an incoming relativistic beam track and a single outgoing relativistic shower track, did not present sufficiently violent appearance to attract our attention. However, the Serpukhov data at(7) 67 GeV indicates an interaction length of 45 m for such events. The Russian group feels that this number is an overestimate because of possible coherent interactions with deflection angles less than 0.6° which have been excluded as elastic scatters in their analysis of 1-prong events. It is clear that the cross-section for 1-prong white stars in emulsion is too large to be ignored. We cannot obtain this number from other members of our collaboration who used the line scanning technique because they too have difficulty in seeing these events.

Therefore we carry out a model dependent estimate for these events which is based upon existing data$^{(8)}$ for the two-body process

$$p + p \to N^*_{1/2} + p;\ N^*_{1/2} \to N\pi,\ N\pi\pi \qquad \text{(I)}$$

and which uses a theory of particle production in nuclei due to Margolis$^{(9)}$. The theory is an application and extension of the Glauber multiscattering theory to the coherent production of particles in medium and heavy nuclei at multi-GeV energies.

We are interested in the process $1 + A \to 2 + A$ (II)

in the high energy limit where the longitudinal momentum transfer

$$q_\ell = \frac{m_2^2 - m_1^2}{p_1 + p_2} \longrightarrow 0 .$$

In this reaction 1 is the incident particle, 2 is the outgoing particle (i.e. $N^*_{1/2}$) and A is the target nucleus in its ground state. Assumptions made are that the interaction does not depend on target quantum numbers, that the two-body process (I) is only a small part of the total pp or $N^*_{1/2}$ total cross-section σ_1 or σ_2 respectively, and that the scattering amplitudes are predominantly imaginary. Then the result for the coherent differential cross-section is$^{(10)}$

$$\frac{d\sigma^{II}}{dt} = \left.\frac{d\sigma^{I}}{dt}\right|_{t=0} \left| \int J_0(qb)\, \frac{e^{-\frac{\sigma_1}{2}T(b)} - e^{-\frac{\sigma_2}{2}T(b)}}{\frac{\sigma_1}{2} - \frac{\sigma_2}{2}}\, d^2b \right|^2 \qquad \text{(i)}$$

Here J_0 is the cylindrical Bessel function of the first kind of order zero, $t \simeq -q^2$ where $\vec{q} = \vec{p}_1 - \vec{p}_2$, and $T(b)$ is a profile function.

$$T(b) = A\int_{-\infty}^{\infty} \rho(b,z)\,dz$$

$\rho(\vec{r})$ is the single particle density function of the nucleus with normalization

$$\int \rho(\vec{r})\,d\vec{r} = 1 .$$

To carry out the calculation we assumed the $N^*_{1/2}$-nucleon cross-section is essentially the same as the nucleon-nucleon cross-section, i.e.

$$\sigma_1 \simeq \sigma_2 \simeq 39 \text{ mb} .$$

Thus the expression (i) becomes

$$\frac{d\sigma^{II}}{dt}\Big/\left(\frac{d\sigma^{I}}{dt}\Big|_{t=0}\right) = \left|\int J_0(qb)\,T(b)\,e^{-\frac{1}{2}\sigma T(b)}\,d^2b\right|^2 \qquad (ii)$$

We assumed Gaussian density functions

$$\rho(\vec{b},z) = \frac{3(6/\pi)^{1/2}}{4\pi R^3}\, e^{-\frac{3}{2}\frac{b^2+z^2}{R^2}}$$

where R is the root-mean-square nuclear radius. Values of R used for the emulsion nuclei were taken from electron scattering data(11) and are given in Table 6.

We obtain

$$T(b) = \frac{3A}{2\pi R^2}\, e^{-\frac{3}{2} b^2/R^2}$$

and for purposes of carrying out the integration in (ii) we transform variables to $y = e^{-3/2\ b^2/R^2}$. The right hand side of (ii) becomes

$$A^2\left|\int_0^1 J_0\left(q\sqrt{-\tfrac{2}{3}R^2 \ln y}\right) e^{-\frac{3A\sigma}{4\pi R^2}y}\,dy\right|^2,$$

which was evaluated numerically.

The curves of $\frac{d\sigma^{II}}{dt}\Big/\left(\frac{d\sigma^{I}}{dt}\Big|_{t=0}\right)$ for two emulsion nuclei are shown in Figure (5). Values at t = 0 are interpreted as the squares of the "effective nucleon number", i.e. as N_{eff}^2. N_{eff} represents the average number of nucleons of the target nucleus which act together to coherently produce 2 in the forward direction. Values obtained for N_{eff} are given in Table 6.

For purposes of calculating the total cross-section for coherent production of 2 it was necessary to integrate the curves discussed above and multiply by experimental values of $\frac{d\sigma}{dt}^{(I)}\Big|_{t=0}$. From the data of reference (8) the dominant contribution is from the N$'(1470)^+$ which has

$$\frac{d\sigma}{dt}\left[N'(1470)^+\right]\bigg|_{t=0} \simeq 12. \ \left(\frac{mb}{GeV^2}\right)$$ (at beam momenta 4.55, 6.06, and 7.88 GeV/c)

The calculated cross sections $\sigma_{N'(1470)^+}$ are shown in Table 6 together with the cross section for p + p → N$'$(1470) + p , measured$^{(12)}$ at 30 GeV.

Of course we are interested only in the decay modes of N$'$(1470) which exhibit one charged track, i.e. $p\pi^o$, $n\pi^+$, $p\pi^o\pi^o$ and $n\pi^+\pi^o$. Since the $N\pi$: $N\pi\pi$ branching ratio is$^{(13)}$ ∿ 60:40 it is reasonable to expect that ∿ 80% of the cross-section contributes to the processes of interest. Thus we can obtain the interaction length from $\lambda = (.8 \times \Sigma n_i\sigma_i)^{-1}$ where the n_i (number of atoms of type i per cm^3) are obtained from Table 1 and the σ_i are given above.

Therefore we crudely estimate the 1-prong white star interaction length to be 32 m, which essentially agrees with the assessment of the Serpukhov data at the beginning of this section.

In Section 5.2, we include this estimate as an entry in the relevant shower particle multiplicity distributions.

4.3 Correction for 2-Prong White Stars

Events with $N_s = 2$, $N_h = 0$ and no recoil are caused by proton-nucleus inelastic interactions, by knock-on electron interactions, and by elastic pp collisions. The number of inelastic events may be extracted from a collection of events from all three categories because cross-sections for knock-on electrons and elastic pp collisions are known. These calculations are done below and applied to our data.

The elastic pp cross-section at 200 GeV is$^{(14)}$ 6.8 ± 0.3mb. From Table 1 the hydrogen content at beam exposure time was .055 gm/cm^3. Thus the mean free path for elastic pp collisions is 44.7 ± 2.0m.

The collision probability for protons (mass m, momentum p, kinetic energy E) incident upon electrons from atoms of charge Z and atomic number A is$^{(15)}$ given by

$$\Phi_{coll}(E,E')dE' = \frac{2\pi N Z r_e^2 m_e \, dE'}{A\,\beta^2 (E')^2}\left[1-\beta^2\frac{E'}{E'_m}+\frac{1}{2}\left(\frac{E'}{E+m}\right)^2\right]$$

Here E' is the recoil electron kinetic energy, N is Avogradro's number, m_e the electron mass, β the incident proton speed, and $r_e = e^2/m_e$ the classical electron radius The recoil electron makes an angle θ with respect to the beam direction related to E' by

$$E' = \frac{2 m_e p^2 \cos^2\theta}{\{m_e + (p^2+m^2)^{1/2}\}^2 - p^2\cos^2\theta}$$

The maximum energy E'_m transferable to the electron is given by E' at $\theta = 0$.

In order to apply this collision probability expression it is necessary to choose a range of E' over which to form $\Phi = \int \Phi_{coll}(E,E')\,dE'$. We chose as upper limit $E' = E'_m$. The lower limit was chosen to correspond to $\theta = 7^\circ$, thus excluding all knock-on phenomena at $\theta > 7^\circ$. Due to shrinkage of emulsion during development this angle is actually measured as $\sim 16^\circ$, and is consequently associated with minimum tracks flat enough to be easily missed, so that such events might not be seen while scanning. Perhaps a more important reason for the choice of this cut-off angle is related to the fact that recoil electrons at 7° have E $\approx$ 68 MeV. Electrons at this and lower kinetic energies are usually recognizable by their twisted tracks caused by multiple Coulomb scattering.

The calculated mean free path for knock-on collisions in the angular range described above is shown in Table 7 for each emulsion element. The total mean free path is obtained from $\lambda = [\Sigma_i 1/\lambda_i]^{-1}$. Thus the knock-on mean free path used for corrections is 2.6 m.

With the intention of testing these knock-on and elastic pp corrections we kept record of all 2-prong clean events while rescanning the 11 mm^2 mentioned in Section 4.1. We found 18 events for an uncorrected mean free path of 2.0 ± .5 m. This is not much different from the correction to be applied.

The correction described above is not very satisfactory for two reasons. First of all, it appears to throw out almost as many events as are measured, so that the result is not accurate unless statistics are very high. Secondly, we wish to present the shower particle angular distribution for $N_h = 0$ events, so that it is important to throw out only events which are supposed to be thrown out.

Therefore in our total sample of 23 mm^2 of emulsion scanned each event was carefully restudied to see if the scattered angles were consistent with elastic pp scattering, or if a track could be seen to wobble like a knock-on electron. Such events were thrown out. The remaining knock-on events were selected on the basis that the proton deflected much less than would be expected in collisions involving heavier particles such as pions. Surviving events were accepted as genuine proton-nucleus inelastic 2-prong clean interactions.

4.4 Correction for 3-Prong White Stars.

Events with $N_s = 3$, $N_h = 0$ and no recoil are caused by proton-nucleus inelastic interactions, by photon produced e^+e^- pairs which are coincident with beam tracks, and by direct e^+e^- pairs produced by beam protons in the electromagnetic field of emulsion nuclei. We shall discuss how the latter two categories were eliminated.

Many high energy photons were created by the decay $\pi^0 \rightarrow 2\gamma$. A fraction of these photons materialize to pairs at points on the tracks left by beam protons. It is hard to estimate the number of such false tridents because the π^0 spectrum is unknown.

However direct identification is possible since the beam track is not deflected and both members of the pair travel in nearly the same direction. In fact the rms angle between the trajectory of the e^+ or e^- and that of the primary photon[(15),p.83] is $\sim \frac{m_e}{E}\ln\left(\frac{E}{m_e}\right)$, where E is the photon energy. For E ∿ 1 GeV this angle is ∿ 0.2°. Events with these characteristics were thrown out.

A calculation[(15),p.86] for direct pair production by beam protons is shown in the Appendix. Interaction lengths for each of the emulsion elements are given in Table 8. We estimate the mean free path for this process to be 3.9 m. While rescanning the 11 mm^2 mentioned in Section 4.1, we kept record of all 3-prong clean events which might be inelastic interactions or caused by direct pair production. We found 10 events corresponding to a mean free path of 3.6 ± 1.1 m. Thus as in the 2-prong case the correction is almost as big as the quantity to be corrected.

Once again we decided our statistics did not warrant such a technique, and considered the possibility of recognizing direct pairs by their strongly scattered tracks. Our biggest problem would come from events in the high energy regions (IIN and IIS in the Appendix) of the calculation. In these regions the energy shared by the pair is greater than $2\frac{m_e}{m_p}$ times the beam energy, that is greater than 0.21 GeV. Table 8 gives the fraction of such events for each element. The total fraction, being ∿ 10% is not very small. We nevertheless decided that direct recognition of the pair production events was the lesser evil.

4.5 Identification of Coherent Events

A coherent reaction between(5) a beam proton and stationary target nucleus must leave the target in a state which cannot in principle be observed to find out which nucleon has been struck. Therefore coherent events in emulsion have no nuclear fragments or visible recoils. Furthermore slow pion production is not expected because an angular coherence criterion (given below) forbids large production angles. Since the target contributes no particle to the shower the visible number of shower particles N_s is odd. The difference in phase shift between the incident proton and outgoing shower states must satisfy the condition $\frac{q_\parallel}{\hbar} R_A \leq 1$. Here $q_\parallel$ is the longitudinal momentum transfer, and R_A is the radius of an emulsion nucleus. By simple kinematics(16) this condition may be written:

$$\sum_i \sin\theta_i \lesssim \frac{\hbar}{R_A m_\pi} \approx A^{-1/3} \sim .2 \text{ to } .4 \text{ (excluding H')} .$$

The sum is over all shower particles produced in the reaction, however we shall apply this condition summing over only those particles which we can see. This is justified by the fact that there are usually less neutral (i.e. unobserved) shower particles than charged shower particles, and because of the approximate nature of the inequality.

As pointed out in the 67 GeV/c results(7) not all clean events of a given N_s with $\Sigma \sin \theta_i \leq 0.3$ are coherent. A background subtraction may be performed by considering the small " dirty " (those with $N_h = 1$, or a recoil, or both) stars of the same N_s. We expect the ratio of these (incoherent) dirty stars with $\Sigma \sin \theta_i \leq 0.3$ to dirty stars with $\Sigma \sin \theta_i > 0.3$ to be approximately the same as the ratio of incoherent clean stars with $\Sigma \sin \theta_i \leq 0.3$ to clean stars with $\Sigma \sin \theta_i > 0.3$. With a total sample of only 10 stars satisfying coherence criteria (at $N_s = 3,5,7$) we lacked sufficient statistics to apply this type of correction, and simply kept all the clean events satisfying the angular coherence criterion. However, when our data is combined with the results of other members of the collaboration for a future publication on coherent events, we shall be able to apply the correction described above.

As a final remark we mention that the angular distribution results in Section 5.4 are a by-product of this $\Sigma \sin \theta_i$ analysis.

4.6 Limitations in Target Nucleus Identification

A drawback in emulsion experiments is the inability to identify the nuclear targets in most reactions. Some information may be obtained by range and track thickness measurements of visible fragment or recoil tracks, but this information is too incomplete and too laborious to obtain to justify the effort. We therefore prefer to accept this limitation and leave the study of interactions with specific nuclei to other experimental techniques [such as bubble chambers filled with He,Ne(17) or organic materials, or counter experiments with nuclear targets surrounded by Cerenkov counters(18)].

Despite this drawback, we compare (in Chapter 6) our results to some models whose predictions can be obtained by averaging over the known emulsion composition. Since these models are only weakly dependent on atomic number it proves useful to divide the emulsion elements into three groups as follows:

H (heavy) : Ag, Br, I
M (medium) : C, N, O
L (light) : H

From the emulsion composition, and assuming an $A^{2/3}$ cross-section dependence, the H:M:L interaction ratios should be ∿ 70%:25%:5%. From the N_h and recoil spectrum in Section 5.3 we can identify most of the interactions from the heavy group.

5. RESULTS

5.1 Inelastic Mean Free Path

Before calculating the interaction length it was necessary to make top and bottom depth cutoffs. To allow the scanner to determine whether or not a beam proton entered an event a top depth cutoff of 22 ± 1.2 μ was found sufficient. The error bar is based on the depth of focus given in Table 3. Event loss of small stars (those with $N_h \leq 1$) near the emulsion bottom was obtained from Figure 6 which shows the number of events scanned versus depth in emulsion. This loss appears connected to the deterioration of object image quality by light scattering through large thicknesses of emulsion. We chose a bottom cutoff of 202 ± 1.2 μ to eliminate this bias. Since the emulsion was 276 ± 2 μ thick on the day this was done, the thickness of undeveloped emulsion used for inelastic mean free path calculation was 421. ± 5 μ of the original 646 μ.

233 out of 279 stars scanned in 23 mm^2 survived these cutoffs. Using an average flux measured for each mm^2, we determined that the stars were found while scanning 7890 ± 100cm of track. Thus the inelastic mean free path is 7890 ± 100cm/233 stars = 33.9 ± 2.3 cm, assuming a statistical standard deviation for the number of stars. Note that this number excludes any events in the category $N_h = 0$, $N_s = 1$, which were not measured. If we use the analysis of Section 4.2 to correct for these events, the mean free path decreases to 33.6 cm.

5.2 Multiplicity Distribution of Shower Particles

Some events included in the inelastic mean free path calculation proved too difficult to classify because of image distortion extending from the interaction vertex down to the emulsion bottom. The distortion was due to large numbers of heavy tracks. By increasing the lower depth cutoff to 100 μ, we were able to exclude these events. The shower distribution of the remaining events is shown in Figure 7. The entry for $N_s = 1$ is based on the discussion in Section 4.2. The average charged particle multiplicity is 13.1 ± .25.

In Figure 8 we present the shower particle distribution for small stars (i.e. those with $N_h \leq 1$) which was obtained by reinstalling the 202μ cutoff to slightly increase our statistics. The hatched distribution corresponds to events with even multiplicity. The average small star charged shower multiplicity is 7.4 ± .4 . For the even prong ("hydrogen-like") events it is 7.8 ±0.6, which is in excellent agreement with the hydrogen bubble chamber(14) pp result of 7.65 ± 0.17. We must recall however that only about 10 of the 25 events used in calculating the average are expected to be pp interactions, based on the emulsion composition. For odd-prong events the average multiplicity is 7.0 ± 0.5. This number is somewhat low because of coherent events at N_s = 3,5 and 7 which tend to lower the average multiplicity.

We found 10 clean (N_h = 0, no recoil) odd-prong events (see Section 5.4 for details) satisfying $\Sigma \sin \theta_i \leq 0.3$ among the 56 small stars. These interactions, which can be coherent, are composed of 7 three-prong, 1 five-prong and 2 seven-prong stars. If we remove these possible coherent events as well as the 2 one-prong coherent events (estimated from the model in Section 4.2) from the 33 odd-prong events in Figure 8 we obtain an average charged shower multiplicity of 8.4 ± .6. The change in multiplicity caused by the removal of these interactions demonstrates the important role which they play in hadron-nucleus collisions at high energy. We remark that the overabundance of three-prong coherent events is in agreement with the 67 GeV(7) results. Our statistics are not sufficient to allow us to determine if there is an overabundance of 5 and 7 prong coherent events.

Figure 9 (a) contains all the events in Figure 7 which are unambiguously caused by beam interactions (i.e. events with $N_h > 8$, or a recoil, or both) with heavy (Ag, Br, I) nuclei. These constitute 120 of 202 events, representing 60% of our sample. This is in reasonable agreement with the 70% estimate based on the emulsion composition(see Section 4.6), and indicates that only approximately 15% of the heavy nucleus interactions cannot be unambiguously identified. The average charged shower multiplicity for these events is 15.1 ± 0.4, which is larger than the value obtained for all the events including the light and medium interactions.

For purposes of comparison consider Figure 9(b) which contains the clean events of Figure 8. These include the coherent events, the collisions with hydrogen nuclei, and any remaining peripheral collisions in which the target nucleus was not visibly disturbed. Here the average shower distribution is only 6.2 ± 0.5 which is less than half as large as the corresponding number for large nucleus interactions. Further aspects of the correlation between star appearance and shower multiplicity will be given in Section 5.3.

Multiplicity distributions play an important role in pp collisions by testing models which predict their energy dependence. Interesting quantities are(19) $< N_s(N_s-1) >$ and $< N_s >/D$ where $D = < N_s^2 > - < N_s >^2$ is the variance (i.e. $D = \mu \equiv < N_s >$ for Poisson distributions). The first expression $< N_s(N_s-1)>$ grows like $\ln s$ or $(\ln s)^2$ in multiperipheral models, and like $\sqrt{s}$ in fragmentation models. Here s is square of the total C. M. energy. The second expression $< N_s >/D$ grows as $(\ln s)^{-1}$ in multiperipheral models, and like $(\ln s)/s^{1/4}$ in fragmentation models. The distribution width may be compared to the Poisson using width parameter $f_2 = <N_s(N_s-1)> - <N_s>^2$, since for the Poisson case $f_2 = D - \mu = 0$. We also mention the empirical relation of Wroblewski,(20) namely $D = 0.585\ (<N_s> - 1)$, which is well satisfied in the pp 20-200 GeV range. Naturally the energy dependences of the distribution parameters used for pp collisions will probably be altered when applied to p-nucleus collisions. Therefore we present these quantities for comparison to the 200 GeV pp(14) values in Table 9. Predictions on the behavior of $< N_s >$ in p-nucleus collisions will be discussed in Chapter 6.

5.3 Multiplicity Distribution of Nuclear Fragments

The events of Figure 7 are replotted as number of events vs. N_h (number of black and grey tracks), shown in Figure 10. The hatched events are those in which a recoil has been observed. We obtain the average value $<N_h> = 7.8 \pm 0.2$. Table 10 gives the percentage of stars in various N_h groups and compares this to data at 22.5 and 6.2 GeV(21). There is an increase of about 16% in the number of events which have $N_h \leq 1$ over the 22.5 GeV data, which can be explained by the overabundance of coherent events.

An increase in shower number with atomic number is evident from a plot of N_h vs. $<N_s>$ as in Figure 11. We fitted this data with a straight line $<N_s> = A+BN_h$. The parameter values are $A = 7.85 \pm .30$, $B = .60 \pm .035$, and the reduced chi-square is 2.90. The intercept A agrees very well with the hydrogen result(14) of $<N_s> = 7.65 \pm .17$. However this should not be taken too seriously because there is no justification in assuming the data should be fitted by a line since events at $N_h = 0$ are biased toward coherent and pp interactions while events at values of $N_h > 8$ are biased toward p-heavy nucleus interactions. Note the low experimental point at $N_h = 0$ of 6.6 ± 0.5. We must recall that the hydrogen multiplicity may be pulled down by the coherent events as well as peripheral quasi-"p-neutron" collisions with neutrons of the target nuclei.

5.4 Angular Distribution of Small Stars

In our sample of 233 stars measured in 78.9m of beam track we found 56 small stars, that is stars which have no more than one heavy track. Using the method of angular measurements described in Section 3.2, the polar angles were measured for all the shower particles, an average of 7 per event. The $\Sigma_i \sin\theta_i$ analysis of Section 4.5 was applied to each clean (i.e. $N_h = 0$ and no recoil) odd N_s event, resulting in $dN/(d\Sigma \sin\theta_i)$ distribution for events seen in Figure 12. We chose the events with $\Sigma \sin\theta_i \leq 0.3$ as coherent, as was discussed in Section 4.5. We find 7 3-prong, 1 5-prong and 2 7-prong possible coherent stars.

Before proceeding we shall introduce the parameters (22) which will be useful in describing the properties of the angular distributions. The basic variable used is $U_L = \log_{10} \tan\theta_L$, where θ_L is the angle in the lab made by a shower particle with respect to the incident beam direction. Let us call this shower particle π and assume that it moves with speed β_π and at an angle θ_C in reference frame C. The reference frame C moves at speed β_C in the same direction as the beam, with a Lorentz factor γ_C. Then the transformation of angles is given by

$$\tan\theta_L = \frac{\sin\theta_C}{\gamma_C\left\{\cos\theta_C + \frac{\beta_C}{\beta_\pi}\right\}}$$

If we assume $\beta_C/\beta_\pi \sim 1$ then we obtain

$$\gamma_C \tan\theta_L \simeq \tan\theta_C/2 \qquad \text{or}$$

$$\log_{10}\tan\theta_L \simeq \log_{10}\tan\frac{\theta_C}{2} - \log_{10}\gamma_C \; .$$

Therefore we obtain the remarkable result that the $\log_{10} \tan\theta_{C/2}$ distribution looks the same as the U_L distribution in any frame where $\frac{\beta_L}{\beta_\pi} \sim 1$ is satisfied. This is expected to be applicable in collisions of sufficiently high energy that the center-of-mass (CM-) frame moves with $B_{CM} \sim 1$ with respect to the lab frame, and a shower particle π moves with $B_\pi \sim 1$ with respect to the CM frame. Consider a choice of the $\log_{10} \tan \theta_{C/2}$ axis such that $< \log_{10} \tan \theta_{C/2} > = 0$. This defines a frame C which is most nearly symmetric with respect to $\theta_C = 90^\circ$. Such a frame is expected to approximate the CM- frame. This forms the basis of the Castagnoli formula(23), $-\log_{10} \gamma_{CM} = \langle \log_{10} \tan \theta_L \rangle$, from which the Lorentz factor γ_{CM} of the CM- frame may be deduced. An effective number N_{eff} of target nucleons which participate kinematically in an average collision may be obtained from the expression

$$\gamma_{CM} = \frac{E_p + N_{eff} m_N}{\sqrt{(E_p + N_{eff} m_N)^2 - P_p^2}}$$

where E_p and P_p are the lab energy and momentum of the beam particle, and M_N is the nucleon mass. Solving for N_{eff}

$$N_{eff} = (P_p/\beta_{CM} - E_p)/m_N \, .$$

Another interesting feature of the variable U_L is its approximate equivalence to the lab rapidity(24) y_{lab}. The relation is

$$U_L \simeq \log_{10} 2 - y_{lab} \, , \; \theta_L \neq 0 \, .$$

From the Castagnoli formula one deduces the average lab rapidity for an event is

$$\bar{y}_{lab} \simeq \log_{10} (2 \gamma_{CM}) \, .$$

The dispersion (or isotropy) σ is defined by:

$$\sigma = \sqrt{\frac{1}{N-1} \sum_i (U_{L_i} - \langle U_L \rangle)^2}$$

is a parameter which is useful in determining the character of the angular distribution. For example, a distribution which is isotropic in the CM-frame is nearly Gaussian in the U_L variable, with $\sigma = .39$. A distribution which is flat$^{(24)}$ in the rapidity variable y_{lab} over a length L (such as the central plateau of the scaling hypothesis) has

$$\sigma^2 = \frac{1}{L}\int_0^L dU_L\left(U_L - \frac{L}{2}\right)^2 = \frac{L^2}{12}$$

The final parameter which we are interested in is $D = \frac{N_e - N_i}{N_e + N_i}$ where N_i is the number of particles lying in the central region $\left|\log_{10}\tan\frac{\theta_{CM}}{2}\right| < 0.674\,\sigma$ and N_e is the number outside this region. Then we expect D to be zero for Gaussian distributions, positive for distributions more populated in the wings, and negative for those with more particles in the central region.

Let us now consider the construction of the U_L distributions about to be presented. The data was collected in U_L- bins of width 0.2. Naturally, errors in the determination of U_L cannot be directly exhibited on the distribution, so we have shown average values for the error bars of some bins in Table 11. These values were computed on the basis of length measurement errors shown in Table 4 and discussed in Section 3.2. For values of U_L smaller than -2.3 the errors became larger than the bin width, reflecting the inaccuracy with which angles smaller than 0.3° are measurable in vertically exposed emulsion plates. Most of the U_L values are between -2.2 and 0.0 so we expect reasonably accurate distributions with errors determined primarily by the statistics.

In Figures 13 and 14, we show the U_L distribution for the following categories of events:

Figure 13: a) all the small stars
　　b) "clean" stars which may be coherent (i.e. $\sum_i \sin\theta_i \leq 0.3$)

Figure 14: a) small stars with $N_h = 0$
　　b) small stars with $N_h = 1$

The dotted line passing through the $U_L = -1.015$ represents 90° in the nucleon-nucleon center of mass system. Table 12 summarizes the number of particles appearing in each distribution, $< U_L >_{CM}$, N_{eff}, σ, D and the fraction $f_{forward}$ of particles which travel forward in the CM-system. Except possibly for the coherent events, the results do not appear to favor an isotropic distribution in the CM- frame. We mostly find that more particles travel backward than forward in this frame, and the angular region defined by $| \log_{10} \tan \theta_{CM/2} | < .64\ \sigma$ is less populated than would be expected in an isotropic distribution. Obvious reasons for these asymmetries are the coherently-produced particles and the surviving incident protons. The presence of asymmetries due to the limiting nature of transverse momentum distributions (fostering & festering ideas such as limiting fragmentation and fireballs) has long been known. The effective nucleon numbers for these distributions are only fractions of one, a fact which can perhaps be related to the peripheral nature of many of the collisions occurring in small events. Further asymmetry is due to the absence of tracks made by neutral particles, particularly target nucleons which constitute over half the targets In any case, interpretation of the results must be taken cautiously because the CM-system of a nucleon-nucleus collision is quite a complicated affair due to the size and structure of the nuclei involved. Factorswhich are not accounted for in the simple kinematics we use,such as Fermi motion, are certainly of considerable importance.

Before further discussing angular shower distributions, we shall consider some preliminary results of our collaboration, which include more statistics in the $N_h = 0$ and $N_h = 1$ angular distributions, as well as distributions for $N_h > 1$.

5.5 Comparison of Some Preliminary Results of the Collaboration

The group(2,3) presented preliminary results (including our data) at conferences in Uppsala and Vanderbilt. We present, discuss and expand upon some of these results which have better statistics than our results alone or which we did not measure at all. The reader is invited to compare results obtained in earlier sections to results given here.

Figure 15 contains N_h vs. number of events distribution. The average value of heavy tracks is $\langle N_h \rangle = 7.8 \pm 0.2$. The hatched distribution consists of stars with $N_h \geq 9$ and recoils, assumed to belong to the AgBr group of heavy stars. From this figure ∿ 2/3 of the events fall in this group, which is consistent with the prediction of 70% based on the emulsion composition and an $A^{1/3}$ nuclear radius dependence.

Figure 16 contains N_s vs. number of events for small stars ($N_h \leq 1$) in the horizontally exposed stacks. The average multiplicity for all events (solid lines) is $\langle N_s \rangle = 8.1$. For events with $N_h = 0$ (dashed lines) $\langle N_s \rangle = 7.6$, which is perfectly consistent with hydrogen data even though peaks at $N_s = 3$ or 5 exist in this data corresponding to coherent production. We must point out that since this graph was published, much remeasurement has taken place to increase statistics and evaluate efficiencies.

Although no figure is available yet, the average-charge multiplicity for all events has been calculated to be $\langle N_s \rangle = 12.9 \pm 0.4$. The average value for heavy stars (Ag or Br) is $\langle N_s \rangle = 14.1 \pm 0.6$. Only the first of these numbers agrees very well with our own results, 13.1 ± 0.3 and 15.1 ± 0.4 respectively.

Table 13 shows a comparison of the 200 GeV results with previous data for incident proton energies of 6.2 and 22.5 GeV(21). There seems little difference between events at 6 GeV and 22.5 GeV, except for an increase in the average number of charged shower particles. Between 22 and 200 GeV there is an increase in star size as well as in shower multiplicity. The average number of grey tracks has however decreased at the higher energy. This might be partially due to a smaller fraction of pions which are produced with sufficiently low energy to exhibit grey tracks. At 22 GeV it was estimated that the average number of grey tracks due to pions in an event with N_s shower particles was given by $< N_g >_{\text{pionic}} \simeq 0.034\ N_s$, which amounts to ~ 0.2 pionic grey tracks in an average collision. At 200 GeV we might expect fewer of these low energy pions, which supports our assumption that the number of charged shower particles is approximately given by the number of minimum-ionizing tracks.

In Figure 17, we present the mean number of shower particles $< N_s >$ vs. the number of heavy prongs N_h. An almost linear relationship is observed. The mean multiplicity in interactions with $N_h = 0$ is 7.72 ± 0.54 which is a good agreement with the value 7.65 ± 0.17 obtained with a hydrogen bubble chamber(14). The figure also shows the ratio between proton-nucleus and proton-proton interactions versus the number of heavy prongs. The same ratio is shown at 22.5 GeV(21), demonstrating a slight increase in intranuclear production due to multiple collisions at the higher energy.

Table 14 shows the percentage of stars in various N_h groups at NAL and CERN energies. All data are obtained by the along-the track method. It is interesting to note the shift of 6% of the events to the group $N_h \leq 1$ at the higher energy. Since the inelastic mean free path at 6-22 GeV is $37.7 \pm .3$cm, i.e. greater by about 2.5 cm than the corresponding value at 200 GeV, the shift noted above seems due solely to an increase of events with $N_h \leq 1$ at 200 GeV. This increase can be attributed to the coherent production processes which are not as pronounced at the lower energies. Furthermore, we may deduce that the amount of energy transferred to the nucleus is independent of the beam energy in high energy collisions.

Figure 18 shows the angular distributions for stars of different sizes as a function of $U_L = \log_{10} \tan \theta_L$. In small stars the majority of particles are emitted in the forward direction. Coherent production and surviving incident protons contribute to this asymmetry. Stars of medium size have roughly symmetric shower particle distributions in the CM- system. In these interactions only a small number of nucleon-nucleon collisions occur. Large stars have an excess of particles emitted backwards in the CM- system. The change in mean value $<U_L>$ with N_h is shown in Figure 19 as well as the change in isotropy σ. The kinematic effective value N_{eff} of nucleons participating in the collision is shown in Figure 20 as a function of N_h. From this figure it becomes clear that large nuclei may have quite a few intranuclear collisions when struck by high energy particles. However, it is also clear that some of the predominantly peripheral events, which are apparently responsible for the low N_{eff} values at the $N_h = 0$ and $N_h = 1$ entries, must also be due to large nuclei. This is obvious because the number of small events greatly exceeds the number expected (based on the emulsion composition) from the hydrogen nuclei.

We conclude this section by mentioning that slight changes in the results may occur as members of the collaboration continue to amass statistics and check their work, but the qualitative features will not change. Unfortunately, we have not been able in this section to display quantitative results on coherent events to compare with our own measurements because members of the collaboration have not yet pooled their data together.

6. COMPARISON TO MODELS OF INTRANUCLEAR PRODUCTION

6.1 Model of Dar and Vary

This model contradicts a fanatic belief held by some elementary particle physicists that collisions in large nuclei cannot be effectively used to study elementary processes. The purpose of this method is to provide a sensitive test to distinguish between current multiparticle production mechanisms (these are discussed in a review paper by Frazer(25)) which are too flexible to allow most experiments to verify or refute them. These production mechanisms fall into two categories. In the first category are models which predict that final multiparticle states are produced in a single step from the colliding particles. These "one-step mechanisms" include multiperipheral, particle-fragmentation and Bremsstrahlung models. The second category contains models in which final multiparticle states are produced long after the collisions by the decay of one or two compound systems created during the initial collision. Such "compound system mechanisms" include diffraction excitation models, the one-, two- and many- fireball thermodynamic models and statistical bootstrap models. Using simplifying assumptions and elementary nuclear optics Dar and Vary(26) have derived analytic expressions for shower multiplicity of hadron-nucleus interactions for each category.

For the one-step mechanism, assumptions are:

i) multiplicities of pp collisions have logarithmic energy dependence

ii) produced multiparticle final states are confined to a narrow forward cone along the beam axis in the lab system

iii) in any cascading stage the produced particles share equal portions (on the average) of the initial energy, and have the same cross-sections for collisions with target nucleons.

Although empirical constants connected with assumption (i) have recently changed since the 200 GeV(14) and 300 GeV(27) bubble chamber results have been released, important features concerning the energy dependence of p-nucleus multiplicities will not have changed. The result of their calculations based on the intranucleus cascading model, is shown in Figure 21(a). The ratio of p-nucleus to pp multiplicity is displayed as a function of atomic weight A for different energies. Using the approximate ratios described in Section 4.6 based on the emulsion composition it is possible to obtain average multiplicities for p-emulsion collisions from this figure.

Consider next compound system mechanisms, specifically diffraction excitation models. Here one of both of the colliding particles are first excited into resonant states having the same quantum numbers, except for spin and parity, and about the same momenta as the original particles. These resonant states are expected to have inverse lifetimes averaging ~100 MeV, so that, at high energies they usually have time to escape the nucleus due to time dilation. Consequently, the result has the same energy dependence in p-nucleus collisions as in pp collisions. Figure 21 (b) shows the p-nucleus to pp multiplicity ratio as a function of A. The curve with $A^{0.33}$ dependence is obtained by assuming an $A^{2/3}$ dependence of p-nucleus cross-sections. However the $A^{0.26}$ curve better fits data for heavy nuclei, and is used to obtain predictions for our emulsion multiplicity results.

It is now clear to see why the model of Dar and Vary may distinguish between one step and compound system production mechanisms. The curves for one-step processes have an almost linear energy dependence for large A compared to the logarithmic dependence of the pp input, whereas the compound system curve has the same energy dependence for all A as for pp interactions. In Figure 21 (c) we again show these curves, now as a function of energy, for p-nuclear emulsion interactions. Also included are experimental points at 6.2, 22.5(21) and 200 GeV (from Section 5.2). The experimental points distinctly favor the compound system. However we must remark that the curve for one-step processes using the intranucleus cascading model is suspect because of the simplifying assumptions earlier stated. In the next section we shall encounter a more detailed treatment of this method which yields results in much better agreement with the measurements.

6.2 Model of Trefil

An intranuclear cascading model has been developed(28) to test scaling at cosmic-ray energies where high-density nuclear targets (such as emulsion) must be used to compensate for low flux of high energy particles. This model uses rapidity distributions for inclusive particle-nucleon reactions as input and calculates the corresponding incoherent distributions and multiplicities for particle-nucleus reactions. The calculations include a cascading scheme to count the number of particles produced in sequences of inelastic collisions at each rapidity value, and the nuclear physics is handled by Glauber theory. Approximations are: (i) all elastic scatterings of produced particles start at the midpoint of the nucleus, (ii) all particles in a given generation of inelastic collisions have the same average energy and (iii) energy conservation in the production of particles is ignored. This last assumption is justified if energy is high enough that rest masses can be ignored, while the first two assumptions are expected to cause errors of a type which either cancel or go away at sufficiently high energy. Details of the theory are given in reference 29 using as an example inclusive π-nucleus interactions with multiperipheral model (i.e. flat rapidity distribution) πp input. The normalization procedures are not clear to us but the results are reasonable. We remark that closure over final nuclear states was used in carrying out the calculation, so that the theory should be compared to a representative sample of <u>all</u> types of incoherent events, i.e. not just small events or not just big ones.

The model has been applied to p-nucleus interactions$^{(30)}$ using a more realistic multiperipheral model rapidity (i.e. not flat in projectile and target fragmentation regions) distribution pp input. The rapidity distribution dN/dy predicted by the model at 200 GeV for p-nucleus collisions ($A \gtrsim 10$) is shown in Figure 22. We obtained an experimental distribution from the U_L distributions of Figure 18 in the following way. Since the five figures are not based on a single sample, the relative area under each curve was calculated by examining our classification data. We obtained the approximate percentage ratios 10:5:25:20:40 for the N_h categories $N_h = 0$, $N_h = 1$, $2 \leq N_h \leq 5$, $5 < N_h \leq 10$, and $10 < N_h$ respectively. After combining all the distributions it was necessary to convert the $U_L = \log_{10} \tan \theta_L$ scale to the $y = \frac{1}{2} \ln \left\{ \frac{E + p_{\parallel}}{E - p_{\parallel}} \right\}$ rapidity variable by using the equation $y = \ln 10 \left\{ \log_{10} 2 - U_L \right\}$. The resulting experimental distribution, after rough normalization for height, is seen in Figure 22. The calculated curve clearly reproduces the essential features of the data, namely build-up of particles at small rapidities, a rapid rise to a peak, and a more gradual descent at larger rapidities. The curve underestimates the data at small y and overestimates it at large y. This can be understood in terms of energy limitations which allow particles to be produced at angles larger than consistent with the Glauber approximation, and which do not permit all the initial total energy to be invested in a single shower particle. Further possible explanations for minor discrepancies between data and curve are: (i) inclusion of deflected beam and target nucleons in the distribution, (ii) breakdown in the equivalence between U_L and y at small angles and (iii) inaccurate input pp rapidity distributions. Except possibly for (iii), these errors should diminish as the model is applied at higher energies.

Finally consider Figure 23, which contains predicted average multiplicities for $A \gtrsim 10$ as a function of energy. At present only an experimental point at 200 GeV may be included in this figure, for lack of unbiased data at higher energies. Since there is good agreement we conclude that one-step pp production processes (treated by an intranucleus cascading model) have much better status than indicated in the last section using the calculations of Dar and Vary.

6.3 Comments on the Model of Margolis

This model calculates particle-nucleus cross sections using particle-nucleon data for specific two-body processes. The theory treats coherent and incoherent particle production using coupled equations of optical model form for the wave functions of the particles. For example we used this theory in Section 4.2 to calculate the mean free path for coherent 1-prong white stars produced by a single intranuclear scatter. The model can also handle cascade (31) processes, although the calculations grow successively more formidable as the generality of the application increases. The application of the model so far employs compound system production processes, which usually allow the produced excited compound states to escape from the nucleus before decaying to the final multiparticle states.

The formalism is presently being extended to predict multiplicities of particle-nucleus reactions using fireballs as the compound states. Quantities required for this task are fireball mass and multiplicity distributions which may be approximated by various models. For instance, see reference (32) for expressions of these differential cross sections obtained by using reggeon contributions in a two-fireball model. When this work is done it will be possible to apply the test of multiparticle production processes suggested by Dar and Vary; this time, however, applying the more refined models of Trefil (for one-step production processes handled by intranuclear cascading method) and Margolis (for compound system production using the optical models).

7. CONCLUSIONS

In the foregoing text we have studied interactions of 200 GeV protons with complex nuclei, establishing reliable numbers for mean free path and average charged particle shower multiplicities, λ_{inel}=33.9 ± 2.3 cm, N_s =13.1 ± 0.3 and N_h =7.8 ± 0.2, respectively. By comparing these results to values obtained at 6.2, 22.5 and 67 GeV(7,21) it is found that the interaction cross section either remains constant or increases slowly with energy. Although the charged shower multiplicity continues to increase, the energy transferred to the nuclear targets appears to be independent of primary energy. The percentage of events exhibiting little nuclear break-up(i.e. stars with no more than one nuclear fragment) has increased from 18% at 67 GeV to 25% at 200 GeV, and indications (based on angular distribution analysis) are that this might be due to an increase in coherently produced interactions. However, definite conclusions on this subject are still not possible for reasons which we shall discuss later. The comparison of shower multiplicity and interaction length with predictions of intranuclear production models has also not been decisive in establishing which broad category of production mechanisms (one-step such as MPM models vs. compound system such as diffractive excitation models) lies closer to the truth.

Although we have measured many other quantities which are displayed in the various tables and figures we urgently stress that results of an exploratory experiment of this nature (i.e. no target nucleus identification or momentum measurements) can only provide very broad and qualitative indications of features exhibited in the processes observed. Therefore we have tried not to abuse the technique by making specific, decisive, but unjustified physical interpretations of these quantities. Before such knowledge can be claimed it will be necessary to obtain: (i) unambiguous dependence of $<N_s>$ on atomic number, (ii) a more reliable calculation of typical models belonging to the two broad categories of production processes mentioned above, and (iii) the specific energy variation (e.g. lnE v.s. $E^{const.}$) of λ_{inel} and $<N_s>$, a difficult project since this variation seems to be slow.

As far as angular distribution analysis, and the separation of coherent from incoherent events is concerned, the biggest limitation of the technique of nuclear emulsions is statistics. It will be necessary in order to get a clearer picture to resort to other experimental methods (streamer chambers, bubble chambers, or counter experiments) in which not just the angles, but also the momenta of the out-going particles are measured so that energy-momentum conditions can be used to delineate events and allow one to make appropriate 4-momentum transfer(t) cuts.

To conclude, the main objective of this experiment was to provide a first glimpse of the interesting physics to be learned from the interactions of 200 GeV protons with complex nuclei. Other experiments must be devised to pursue various domains uncovered here.

APPENDIX

Direct Pair Production by Charged Particles(15)

Let $X(E,E')\,dE'dx$ represent the probability for the production in dx(gm/cm^2) of matter of a pair with energy between E' and $E' + dE'$ by a singly charged particle of mass m and kinetic energy E, irrespective of the energy division between the e^+e^- pair.

Let U be the energy of the incident particle, U' the total energy of the pair , and set $v = U'/U$. Then define

$$X(E,E') = \frac{8}{\pi}\alpha^2 \frac{N}{A} Z^2 r_e^2 L(U,v)$$

Here $\alpha = 1/137$, N is Avogadro's number, and $r_e \doteq e^2/m_e$. Z and A are the atomic number and charge of the matter being traversed by the incident particle.

Approximate expressions for $L(U,v)$ are known in the low and high energy limits for the cases of no electron screening and complete electron screening. In the second case the Coulomb potential of the nucleus is damped by an exponentially decreasing factor. Each of these four expressions contains undetermined constants which may be chosen by matching the various expressions for L at the boundaries between the different regions. The regions which are of interest to us have the following energy intervals (expressed in terms of v):

IS : $\frac{2m_e/U}{\alpha Z^{1/3}} < v < \frac{2m_e}{m}$ (pair of low energy, complete shielding)

IIS: $\frac{2m_e}{m} < v < \left(\frac{2m_e}{m}\right)\alpha Z^{1/3}\left(\frac{U}{m}\right)$ (pair of high energy, no shielding)

IIN: $\left(\frac{2m_e}{m}\right)\alpha Z^{1/3}\left(\frac{U}{m}\right) < v < 1$ (pair of high energy, complete shielding)

There is also a fourth region corresponding to pairs of low energy, no shielding, the energy is $\frac{2m_e}{U} < v < \frac{2m_e/U}{\alpha Z^{1/3}} \approx \frac{(0.14\ \text{GeV})/U}{Z^{1/3}}$.

Pairs in this energy range do not have sufficient energy to display the straight tracks characteristic of shower particles. Therefore we give only expressions for the other three regions. For the reader's benefit, we have integrated them over the appropriate ranges in v.

$$\text{IS}: \int L(U,v)\,dE' = -\frac{7}{18}\ln\left(\frac{k_2'}{\alpha Z^{1/3}}\right)\ln^2\left(\frac{m U'}{m_e k_2 U}\right)\Bigg|_{\frac{2m_e}{\alpha Z^{1/3}}}^{U' = 2\frac{m_e}{m}U}$$

$$\text{IIS}: \int L(U,v)\,dE' = -\frac{1}{2}\left(\frac{m_e}{m}\frac{U}{U'}\right)^2\left\{\frac{1}{2} + \ln\left(\frac{k_3}{\alpha Z^{1/3}}\frac{m}{m_e}\frac{U'}{U}\right)\right\}\Bigg|_{2\frac{m_e}{m}U}^{U' = 2\frac{m_e}{m}\alpha Z^{1/3}\frac{U^2}{m}}$$

$$\text{IIN}: \int L(U,v)\,dE' = -\frac{1}{2}\left(\frac{m_e}{m}\frac{U}{U'}\right)^2\ln\left(2k_4\frac{U}{m}\right)\Bigg|_{2\frac{m_e}{m}\alpha Z^{1/3}U^2/m}^{U' = U}$$

The various constants k and k' are of the order of 1 and may be chosen $k_2 = 3, k_2' = 1, k_3 = k_4 = 1$. Due to the logarithmic nature of the functions where they appear, the calculation is reasonably insensitive to the choice made.

If the material traversed by the particle has a density ρ(gm/cm^3) of the element under consideration, then the interaction length is given by

$$\lambda = \frac{1}{X(U)\rho}\ , \quad X(U) = \int X(E, E')\,dE' .$$

The results for each emulsion element are given in Table 8.

REFERENCES

1. E. Fiorini, in Proceedings of the Topical Seminar on: Interactions of Elementary Particles with Nuclei (Trieste, September 15-17, 1970), p.241.

2. J. Hebert et al., Study of Nuclear Interactions of 200 GeV Protons in Emulsion, paper presented at Fifth International Conference on High-Energy Physics and Nuclear Structure, Uppsala, Sweden, 18-22 June, 1973.

3. J. Hebert et al., 200 GeV Proton Interactions in Nuclear Emulsion, paper presented at the International Conference on New Results on Multiparticle Production at High Energy, Vanderbilt, ed. R. Panvini (April 1973)

4. W. H. Barkas, Nuclear Research Emulsions (Academic Press, 1963), vol.1 Sections 3.5, 7.2.

5. H.H. Bingham, in Proceedings of the Topical Seminar on: Interactions of Elementary Particles with Nuclei (Trieste, September 15-17, 1970), p.37.

6. E. H. S. Burhop, in the 1962 Easter School for Physicists: Using the Nuclear Emulsion Technique in Conjunction with the CERN Proton Synchrotron and Synchro-Cyclotron (St. Cergue, April 8-18, 1962), p. 275.

7. M. G. Antonova et al., Physics Letters 39B, No. 2 (1972) 282.

8 O. Benary, L. Price and G. Alexander, NN and ND Interactions (Above .5 GeV/c) -A Compilation (UCRL-20000 NN August, 1970).

9. B. Margolis, Nuclear Physics B4,(1968) 433-438.
B. Margolis, Phys. Letters 26B, (1968) 524.

10. K. S. Kolbig and B. Margolis, Particle Production in Nuclei and Unstable Particle Cross-Sections, CERN Pub. 68/482/5-TH. 894 (1968).

11. R. Hofstadter, Revs. Mod. Phys. 103, (1956), 1454.

12. Anderson et al., Phys. Rev. Letters 16, (1966), 855.

13. N. Barash-Schmidt et al., Review of Particle Properties, Rev. Mod. Physics 45, No. 2, Part II (April 1973).

14. G. Charlton et al., Phys. Rev. Letters 29, No. 8 (1972), 515.

15. Bruno Rossi, High-Energy Particles (Prentice-Hall, 1952) pp. 15, 83,86.

16. C. M. Fisher, Il Nuovo Cimento 27, N.4 (1963) 761.

17 F. R. Huson, D. J. Miller and J. S. O'Neall, Nuclear Physics B8 (1968), 391-401.

18. W. Busza, J. I. Friedman, H. W. Kendall and L. Rosenson, A Study of the Average Multiplicty and Multiplicity Distributions in Hadron-Nucleus Collisions at High Energies, NAL Proposal No.178.

19. S. N. Gangoli and P. K. Malhotra, Physics Letters 42B No. 1 (1972) 88.

20. A. Wroblewski, Remarks on Current Models for Charged Multiplicity Distributions (Contributed Paper No. 57 at the XVI International Conference on High Energy Physics (NAL, 1972).

21. H. Winzler, Nuc. Phys. 69 (1965) 661-694.

22. J. Gierula, Experimental Information About Multiple Meson Production at Super-High Energies, Report of the Institute of Nuclear Physics, Cracow (1970).

23. C. Castagnoli, G. Cortini, C. Franzinetti, A. Manfredini and D. Moreno, Nuovo Cimento 10 (1953) 1539.

24. A. Krzywicki and B. Petersson, Phys. Rev. D6, No. 3(1972) 924.

25. W. R. Frazer *et al.*, Reviews of Modern Physics 44 (1972)284.

26. A. Dar and J. Vary, Phys. Rev D6, No.9 (1972) 2412

27. F. T. Dao *et al.*, Phys. Rev. Letters 29, No. 24 (1972) 1627.

28. P. M. Fishbane J. L. Newmeyer and J. S. Trefil, Phys. Rev. Letters 29, No. 10 (1972) 685.

29. P. M. Fishbane , J. L. Newmeyer and J. S. Trefil, SLAC-PUB-1174 (TH) and (EXP), January 1973.

30. P. M. Fishbane and J. S. Trefil, ITB-SB-73-15 (March 1973).

31. G. Von Bochmann and B. Margolis, Nuclear Physics B14, (1969) 609-618.

32. B. Margolis and W. J. Meggs, Lett. Al. Nuovo Cimento V N.10 (1972) 413.

TABLE 1

Emulsion composition

Element	A	Z	N(atoms/cc) (x 10^{20})	Density(gm/cc)
Ag	107.87	47	98.65	1.767
Br	79.90	35	98.06	1.301
I	126.90	53	0.555	0.012
C	12.01	6	134.89	0.269
H	1.008	1	328.59	0.055
O	16.00	8	100.31	0.267
N	14.01	7	30.96	0.072
S	32.06	16	1.28	0.007

Total density = 3.75 gm/cc

Total N = 793.3 x 10^{20} atoms/cc

Average Z = 12.95

Average A = 28.46

TABLE 2

Microscope and power supply specifications

Instrument	Manufacturer	Type	Specifications
Microscope	E. Leitz-Wetzlar	Ortholux	Serial No. 388889
Power Supply	E. Leitz Wetzlar	310-210.001	Serial No. 4284 DO, 501/60 HZ Prim. V 110/120/130/220/230/240, Sec. V 2....10/8 Sec. A 6/1.2

TABLE 3

Optics and optical paramters

Objective	Working distance	N. A.	Maximum Resolution (μ) ($\lambda \simeq 5200$ Å, green light)	Δ (μ)	Ocular	Purpose
Leitz 24x (air)	$\sim 750\mu$	0.65	.4	1.1	15x	Event scanning
Leitz KS FI 53x (oil)	1000μ	0.95	.3	.8μ	8x	Event scanning
					10x	Track classification
					15x	Track Classification and angle measurements

TABLE 4

Errors encountered in angle measurement procedure using 53 x objective in green light.

Quantity measured	Sources of error	Error
X, Y	Scale calibration	0.5 (%)
	Optical resolution	0.3 (μ)
	Grain diameter	∿ 0.5 (μ)
Z	Location of vertex	∿ 1.5 x S (μ)
	Depth of focus	0.8 (μ)

TABLE 5

Rescan of 11 mm^2 at half the initial speed for efficiency purposes.

Star categories	N_1 (scan A and B)	N_2 (scan A only)	N_3 (scan B only)	Total
$N_h = 0$, $N_s = 2$	0	0	2	2
$N_h = 0$, $N_s = 3$	2	0	2	4
$N_h = 0$, $3 < N_s < 7$	3	0	8	11
$N_h = 0$, $7 < N_s$	5	0	1	6
$N_h = 1$, any N_s	10	0	3	13
$1 < N_h$, any N_s	93	0	0	93
Totals	113	0	16	129

TABLE 6

Cross sections for $N'(1470)^+$ production, N_{eff} and rms radii used for Gaussian nuclear density function.

Element	R_{rms} (fm)	N_{eff}	$\sigma_{N'(1470)^+}$ mb
H'	-	1.	0.74 ± .4 *
C^{12}	2.37	5.2	3.9
N^{14}	2.4	5.5	4.1
O^{16}	2.5	6.1	4.5
Br^{80}	4.1	17.8	12.
Ag^{108}	4.5	21.6	14.

* The value of $\sigma_{N'}$ for H is from reference 12.

TABLE 7

Knock-on electron mean free paths for $\theta < 7^o$.

Element	λ (m)
Ag	5.85
Br	7.20
C	33.3
N	125.
O	33.6
H	81.5
Emulsion	2.6

TABLE 8

Estimate of direct pair production interactions lengths

Element	λ (m)	Fraction of pairs in high energy regions (E_{pair} > 0.2 GeV)
Ag	6.1	9 %
Br	11.8	10 %
C	475.	17 %
N	1450.	16 %
O	355.	15 %
H	15000.	41 %
Emulsion	3.9	9.5%

TABLE 9

Parameters for shower multiplicity distributions

Interaction	Criteria	Source of data	$<N_s>$	$<N_s(N_s-1)>$	$D = <N_s^2> - <N_s>^2$	$f_2 = <N_s(N_s-1)> - <N_s>^2$
p-emulsion	all events	Fig. 7	13.1 ± 0.25	214.9 ± 18.	57.4 ± 6.8	44.3 ± 6.6
p-emulsion	$N_h \leq 1$	Fig. 8	7.4 ± 0.4	65.5 ± 11.2	18.5 ± 4.5	11.1 ± 4.3
p-emulsion(Ag,Br,I)	$N_h > 8$ or recoil	Fig. 9a	15.1 ± 0.4	274. ± 26.9	61.5 ± 9.2	46.4 ± 8.9
p-emulsion(clean stars)	$N_h = 0$ and no recoil	Fig. 9b	6.2 ± 0.5	52.6 ± 17.5	20.4 ± 9.2	14.2 ± 8.6
p-p (200 GeV)	-	Ref. 14	7.65 ± 0.17	65.96*	15.09 ± 0.74	7.44 ± 0.72

---

* Since this quantity was not published in Reference 14 we did not insert error bars.

TABLE 10

Comparison of heavy track distributions at 6.2, 22.5(21) and 200 GeV.

Primary Energy (GeV)	$\langle N_h \rangle$	Percentages in various N_h groups $N_h \leq 1$	 $2 \leq N_h \leq 5$	 $5 < N_h$
6.2	9.25 ± 0.18	16.1 ± 1.0	28.3 ± 1.4	55.7 ± 2.2
22.5	8.60 ± 0.25	21.3 ± 1.7	29.3 ± 2.1	49.4 ± 2.9
200.	7.8 ± 0.2	24.8 ± 3.5	29.2 ± 3.8	46.0 ± 4.8

TABLE 11

Approximate errors of U_L in various bins of width 0.2

U_L-bin	$U_L = \log_{10}\tan\theta_L$	ΔU_L
-1.0,-1.2	-1.1	0.01
-1.2,-1.4	-1.3	0.02
-1.4,-1.6	-1.5	0.03
-1.6,-1.8	-1.7	0.05
-1.8,-2.0	-1.9	0.07
-2.0,-2.2	-2.1	0.12
-2.2,-2.4	-2.3	0.18
-2.4,-2.6	-2.5	0.30
-2.6,-2.8	-2.7	0.45
-2.8,-3.0	-2.9	0.72
-3.0,-3.2	-3.1	1.2
-3.2,-3.4	-3.3	1.8
-3.4,-3.6	-3.5	2.8

TABLE 12

Angular distribution parameters for Figures 13 and 14

Parameter	$N_h \leq 1$ (Fig. 13a)	Possible coherent events (Fig. 13b)	$N_h = 0$ (Fig. 14a)	$N_h = 1$ (Fig. 14b)
Number of shower tracks	413	40	227	186
$\langle U_L \rangle$	-1.37 ± 0.06	-1.97 ± 0.22	-1.42 ± 0.08	-1.32 ± 0.08
σ	0.64	0.47	0.68	0.58
γ_{CM}	23.6 ± 3.3	93.3 ± 47.3	26.3 ± 4.8	20.7 ± 3.8
N_{eff}^{*}	.19 ± 0.05	.01 ± 0.01	.15 ± 0.06	.29 ± 0.09
D	-0.03	0.10	0.07	0.01
$f_{forward}$	0.49 ± 0.02	0.48 ± 0.08	0.51 ± 0.03	0.48 ± 0.04

---

[*] This is not the same N_{eff} as the quantity defined in Section 4.2, but is the kinematically effective number of target nucleons(defined in Section 5.4) characteristic of each distribution. The small values of these numbers might be interpreted as being characteristic of collisions with virtual pions at the periphery of the nucleus. In the case of coherent events the $\sum \sin\theta \leq 0.3$ criterion biases angles (and therefore N_{eff}) to small values. A more pessimistic explanation is the possible admixture of electromagnetic interactions among the 2 and 3 prong events, despite the precautions described in Sections 4.3 and 4.4. However this argument cannot be applied to the case N_h=1 which also has small N_{eff}.

TABLE 13

Comparison of events at 6.2,22.5 and 200 GeV

E (GeV)	$<N_b>$	$<N_g>$	$<N_s>$
6.2	5.68 ± 0.21	3.58 ± 0.11	3.3 ± 0.1
22.5	5.22 ± 0.29	3.38 ± 0.14	6.5 ± 0.3
200	5.0 ± 0.1	2.79 ± 0.15	12.9 ± 0.15

TABLE 14

Percentage of stars in various N_h groups

E (GeV)	$N_h \leq 1$	$2 \leq N_h \leq 5$	$5 < N_h$
6.2	16.1 ± 1.0	28.3 ± 1.4	55.7 ± 2.2
22.5	21.3 ± 1.7	29.3 ± 2.1	49.4 ± 2.9
200	27.3 ± 1.6	27.6 ± 1.6	45.1 ± 2.2

FIGURE CAPTIONS

Figure 1 Experimental area for 200 GeV proton-emulsion experiment.

Figure 2 Example of an event scanning sheet.

Figure 3 Example of a track classification sheet.

Figure 4 Example of an angle measurement sheet. The event shown had 23 shower tracks. Angles were calculated by forming the dot product between beam and shower directions. Values of Z on this sheet had to be corrected for the shrinkage factor, while values of X and Y had to be corrected by a conversion factor of 1.717 μ/scale division (±0.5%). Errors propograted in the calculations are based on Table 4.

Figure 5 Differential cross section for coherent production of $N^*_{1/2}$ resonances in units of the forward pp production differential cross section. The curves are for two typical emulsion elements C^{12} and Ag^{108}. The calculation is contained in Section 4.2, with parameters given in Table 6.

Figure 6 Histogram showing the correlation between events scanned and the depth in developed emulsion (from the top) at which they were found. The upper distribution contains 279 stars scanned. 59 of these were small stars ($N_h \leq 1$), shown in the hatched distribution. Loss of small stars at great depths is evident. The dotted line through 202 μ represents the bottom depth cut-off chosen for the interaction length calculation. One small star at 202 ± 2μ was kept, so that 233 events (including 56 of the small stars) survived the cut-off.

Figure 7 Shower multiplicity distribution of 202 events which survived the track classification lower cut-off of 100 μ (from the bottom). The entry at $N_s = 1$ is an estimate based on the model-dependent calculation of Section 4.2. It is not used in obtaining the average charged shower number.

Figure 8 Shower multiplicity distribution of the 56 small stars ($N_h \leq 1$) which survived the cut-off of Figure 6. The entry at $N_s = 1$ is as described above in Figure 7.

Figure 9 a) Shower multiplicity distribution of 120 events involving heavy nuclear targets (i.e. $N_h > 8$ or a recoil observed). These were found among a total sample of 202 events.

b) Shower multiplicity distribution of 31 clean stars ($N_h = 0$, no recoil) found among a to[illegible] sample of 233 events.

Figure 10 Charged nuclear fragment distribution of 202 stars. The hatched distribution corresponds to events in which a recoil has been clearly observed. There are 120 stars which either have recoils, or are to the right of the dotted line. These are assumed to be caused by interactions with heavy (Ag, Br, I) nuclei.

Figure 11 Linear correlation between $< N_s >$ and N_h. The fit is given by $< N_s > = (7.85 \pm 0.30) + (0.60 \pm 0.04)\ N_h$; with a reduced chi-squared of 2.90. The $\langle N_s \rangle$ intercept agrees with the pp point of 7.65 ± 0.17(14). However this agreement is probably not significant in view of the bias towards heavy stars in the region $N_h > 8$. The low value at $N_h = 0$ is due to the dominance of three-prong coherent events.

Figure 12 Selection of possible coherent events based on the $\Sigma \sin\theta \leq 0.3$ test. Of 13 clean 3, 5, and 7-prong events 10 survived. These include seven 3-prong events which all had $\Sigma \sin\theta < 0.1$.

Figure 13 a) $U_L = \log_{10} \tan\theta_L$ distribution for 56 small ($N_h \leq 1$) stars. In this figure and Figure 14, the dotted line corresponds to 90° in the pp CMS.

b) U_L distribution for the 10 possible coherent events shown in Figure 12.

Figure 14 a) U_L distribution of 35 stars with $N_h = 0$.

b) U_L distribution of 21 stars with $N_h = 1$.

Figure 15 N_h multiplicity distribution from Reference 3. The dotted line is a correction for lost events, while the shaded distribution corresponds to stars with $N_h < 10$ having a recoil.

Figure 16 N_s multiplicity distribution for stars with $N_h \leq 1$. Dashed lines: $N_h = 0$; Solid lines: $N_h = 0$ or 1. This figure is from Reference 3.

Figure 17 Mean number of shower particles $< N_s >$ versus the number of heavy prongs N_h, taken from Reference 2. The figure also shows the ratio between the multiplicities in p-emulsion and pp interactions versus the number of heavy prongs. Points at 22.5 GeV are from Reference 21.

Figure 18 U_L distributions for 5 different N_h groups taken from Reference 2. The dotted line through $U_L = -1.016$ corresponds to 90° in the nuclei nucleon CMS.

Figure 19 Variation in $< U_L >$ and the isotropyσ with N_h. The line through $\sigma = 0.39$ corresponds to an isotropic distribution in the nucleon-nucleon CMS. The figure is from Reference 2.

Figure 20 Variation of N_{eff} with N_h based on information from Figure 18. This N_{eff} is a parameter describing angular distributions which is defined in Section 5.4. It is not the quantity of the same symbol used in Section 4.2.

Figure 21 a) Ratio of average particle multiplicy in proton-nucleus collisions, based on the intranucleus cascading model of Reference 26, to the measured average multiplicity in pp collisions as a function of incident energy and atomic number of the nucleus.

b) Ratio of the average particle multiplicity in proton-nucleus collisions, based on the diffractive excitation model of Reference 26, to the measured average multiplicity in pp collisions as a function of atomic number of the nucleus.

c) The ratio of a) and b) is again exhibited, now for proton-emulsion collisions, as a function of incident energy. The line corresponds to the prediction of diffractive excitation models (DEM) while the other curve corresponds to intranuclear cascading models (ICM). The experimental points are from Reference 21 and Section 5.2. Although the DEM calculation is favored, a more careful ICM calculation by Trefil(30) yields good agreement with experiment (see Figure 23).

Figure 22 Rapidity distribution dN/dy: here y is the usual rapidity defined in Section 6.2. The smooth curve is the predicted shape from Reference 30, which we compare to data obtained by the procedure described in Section 6.2.

Figure 23 Charged multiplicity distributions for proton-nucleus collisions taken from Reference 30. The upper curve is the prediction for A $\gtrsim$ 10, while the lower curve is for pp collisions. The experimental point, from Section 5.2, is the multiplicity in p-emulsion collisions at 200 GeV incident energy.

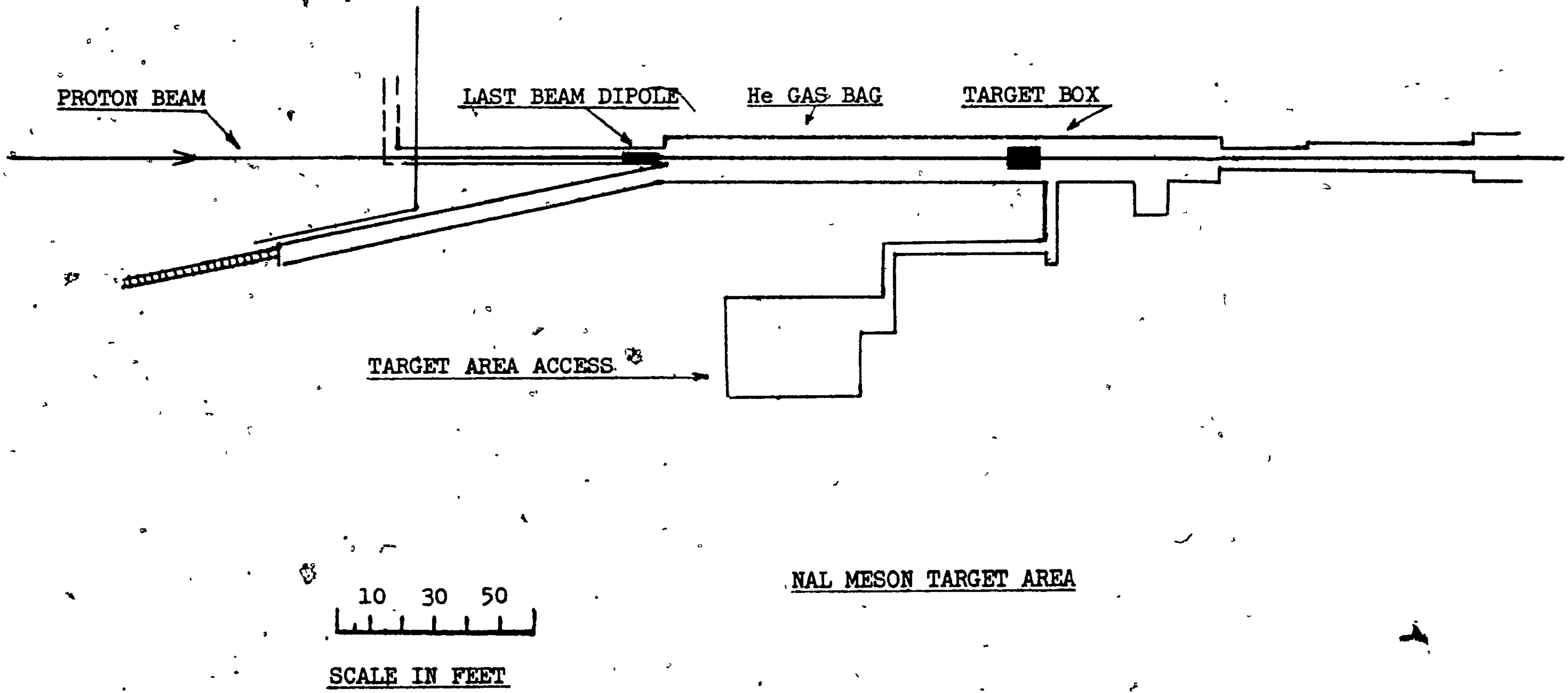
PROTON BEAM
LAST BEAM DIPOLE
He GAS BAG
TARGET BOX
TARGET AREA ACCESS
NAL MESON TARGET AREA
10 30 50
SCALE IN FEET

FIG. 1

Date 20/1/73 No. 1C Plate V8 Scanner G.H.

Method: ☑ standard (i.e. as on 10-11/11/72)
☐ Not standard: Why? (Comments on reverse side, if any)

Grids:

2P 20	2Ⅎ 20
2P 4d	2Ⅎ 4d

Flux:
(area 158×158 μ²) →

										Row totals
4	0	2	2	2	3	3	2	2	2	22
0	3	1	3	4	0	5	4	3	4	27
4	3	0	1	4	0	4	3	3	1	23
6	2	4	4	1	7	3	0	4	1	32
2	5	3	4	2	2	3	1	2	2	26
2	0	3	2	1	3	5	2	3	1	22
1	2	3	2	3	4	2	1	0	5	23
5	1	1	2	5	1	2	5	3	1	26
2	2	1	0	1	3	1	2	2	2	16
6	2	3	2	0	1	4	3	2	1	24

TOTAL: 241

total depth: 275μ

Stars:
(Number each as found)

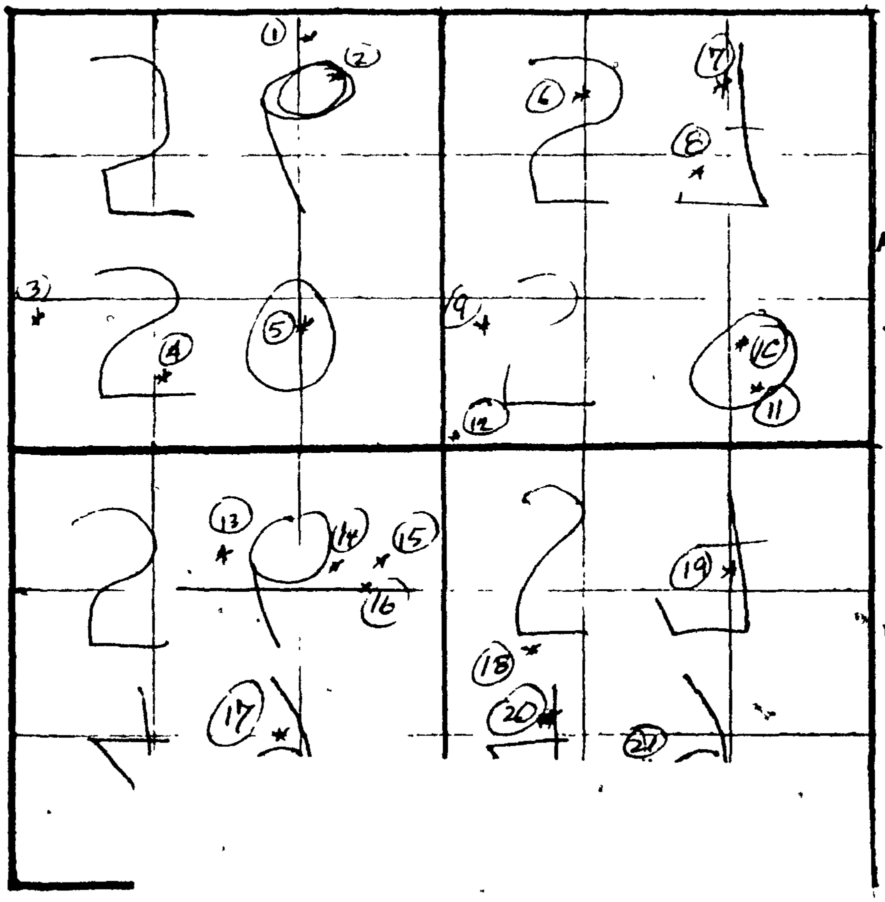

Description (depth, sure star, maybe, size)

✓ ① 29FT, 3B
MB ② OBOG 2 Shower
80FT, δ-ray ?
✓ ③ ~10 heavy, 50FB
X ④ OBOG 2 shower
100 FB, δ-ray ?
✓ ⑤ 75FB, 6B
X ⑥ pair from π° decay
✓ ⑦ 35FB, ~6B
✓ ⑧ 65FT, 3B
✓ ⑨ 44FT, ~7B
✓ ⑩ 70FT, ~5B
X ⑪ 19FT, 1B, only 19μFT
✓ ⑫ 103FB, OBOG 7 shower
✓ ⑬ 100μFT, ~15BγG
120FT 3B,
39FT, δ-ray OBOG2sta
~15BγG

Total Sure: 15
Total Maybe: 2

MB ⑭ 55FT, OBOG 3
✓ ⑰ 182FT, 3BγG
✓ ⑳ 101FT, OBOG

FIG. 2

Plate V8

(xxvii)

Multiplicity Record:

Scanner: G.H.

(June 9, depth = 216μ, cutoff = 175μ FT)

No. Star	Black	Grey	Forward Shower	Transverse Shower	Recoil
27_6 113μFT	6 6 4 3 19	3 1 5 3 12 also e⁺e⁻ pair	8 4 3 6 21	7 6 3 8 24 ⇒ shower = 45	yes
27_{12} 116μFT	2 2 2 1 7	0 0 1 2 3	2 0 4 2 8	1 1 1 1 4 ⇒ shower = 12	yes
27_{15} 187μFT	—	TOO	LOW	— ⇒ shower =	—
27_{16} 155μFT	2 1 0 0 3	0 0 2 (e⁺e⁻) 0 2	1 2 2 3 8	≈90° 1 0 1 1 3 ⇒ shower = 11	yes
27_{20} 98μFT	8 4 2 6 20	—	[illegible]	3 2 4 4 13 ⇒ shower = 26	no

FIG. 3

Scanner: G.H. Date: 25/7 Page: 12 Total Depth: 273

Star	Nh	ΔZ	Z	X_s	Y_s	track	X_s	Y_s	θ(rad)	Δθ	sinθ	$\log_{10}\tan\theta$
26_7	23	1.5	100	-3.4	-1.3	1	.5	-1.3	.28E-1	.3E-2	.28E-1	-.155E1
						2	0.	-1.8	.25E-1	.3E-2	.25E-1	-.160E1
						3	-1.4	-2.8	.18E-1	.3E-2	.18E-1	-.174E1
						4	-3.	-4.1	.205E-1	.3E-2	.205E-1	-.169E1
						5	-5.1	-1.9	.131E-1	.3E-2	.131E-1	-.188E1
						6	-5.2	-2.7	.165E-1	.3E-2	.165E-1	-.178E1
						7	-8.0	-3.0	.355E-1	.3E-2	.355E-1	-.145E1
						8	-1.9	-10.3	.66E-1	3E-2	.66E-1	-.118E1
						9	1.0	-5.	.417E-1	.3E-2	.417E-1	-.138E1
						10	4.0	-3.8	.57E-1	.3E-2	.57E-1	-.125E1
			50	-	-	11	42.	11.	.589	.2E-1	.555	-.176
						12	6.8	8.	.175	.8E-2	.174	-.753
						13	-4.0	27.	.3837	.14E-1	.374	-.394
						14	-8.0	12.	.202	.9E-2	.201	-.688
						15	-28.5	19.	.447	.16E-1	.432	-.320
						16	-48.	6.6	.590	.2E-1	.556	-.174
						17	-27.5	3.0	.358	.14E-1	.354	-.426
						18	-18.	-1.0	.231	.11E-1	.229	-.629
						19	-9.0	-2.5	.109	.7E-2	.108	-.963
						20	24.	-19.	.432	.15E-1	.419	-.336
						21	11.	-1.3	.183	.8E-2	.182	-.732
						22	19.5	-0.6	.300	.1E-1	.296	-.509
						23	12.5	+0.3	.2046	.8E-2	.203	-.683

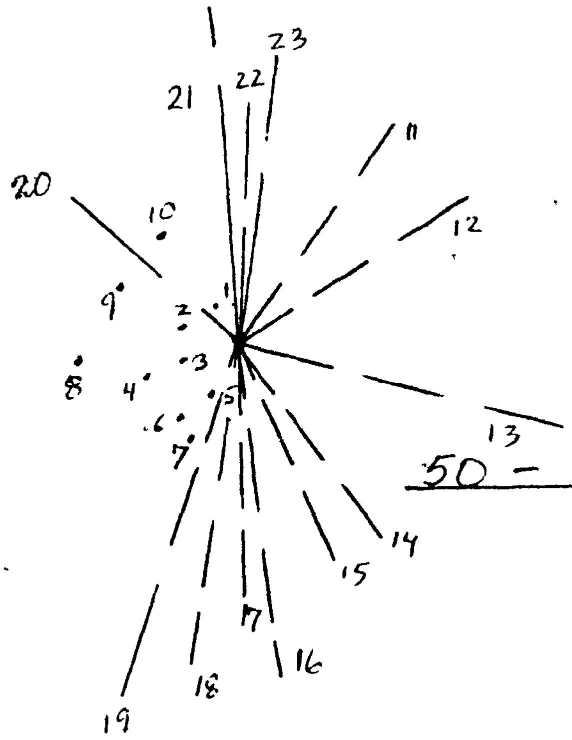

FIG. 4

FIG. 5

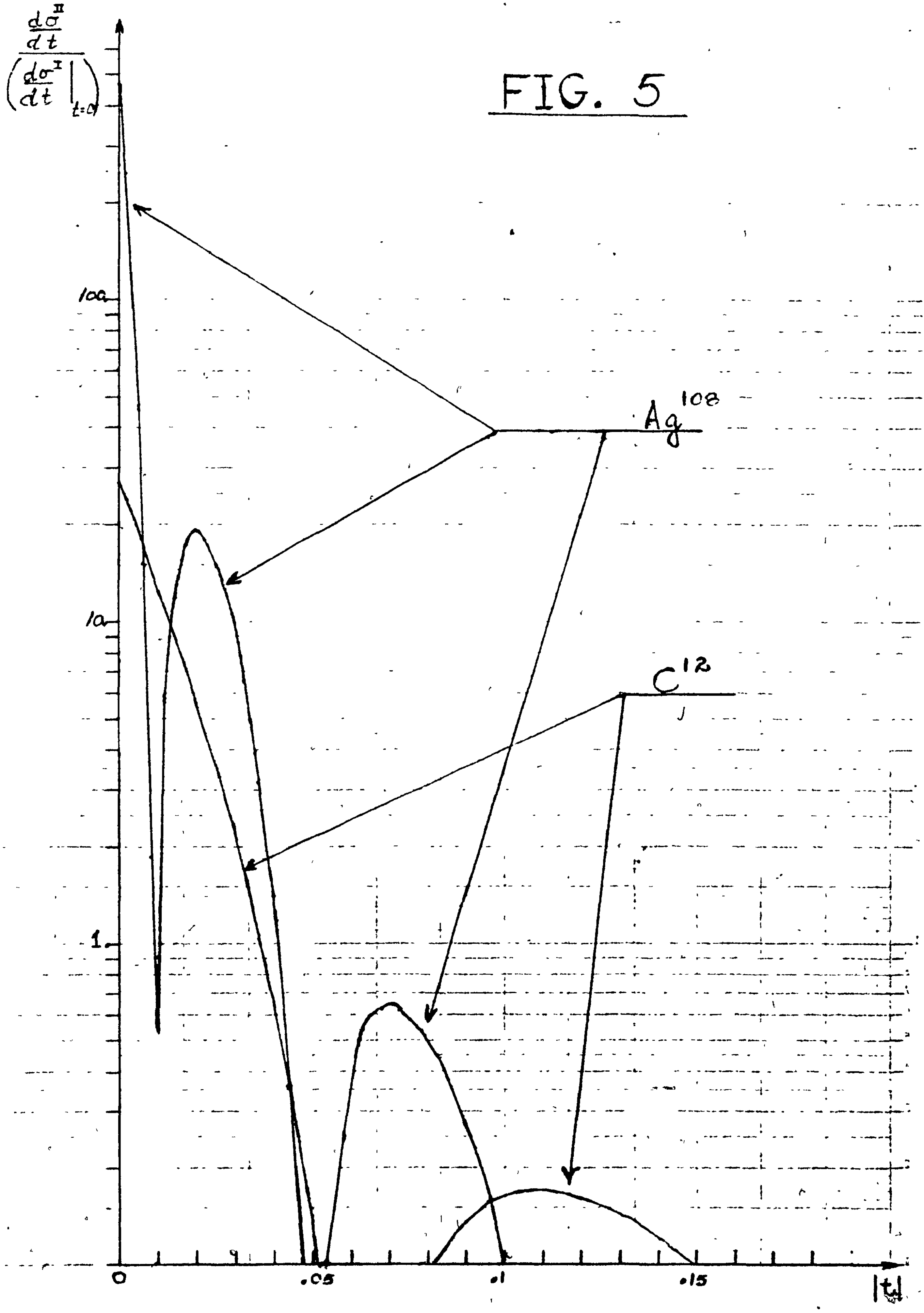
$\dfrac{d\sigma^{II}/dt}{\left(\frac{d\sigma^{I}}{dt}\Big|_{t=0}\right)}$
100
10
1
0
.05
.1
.15
|t|
Ag^{108}
C^{12}

FIG. 6

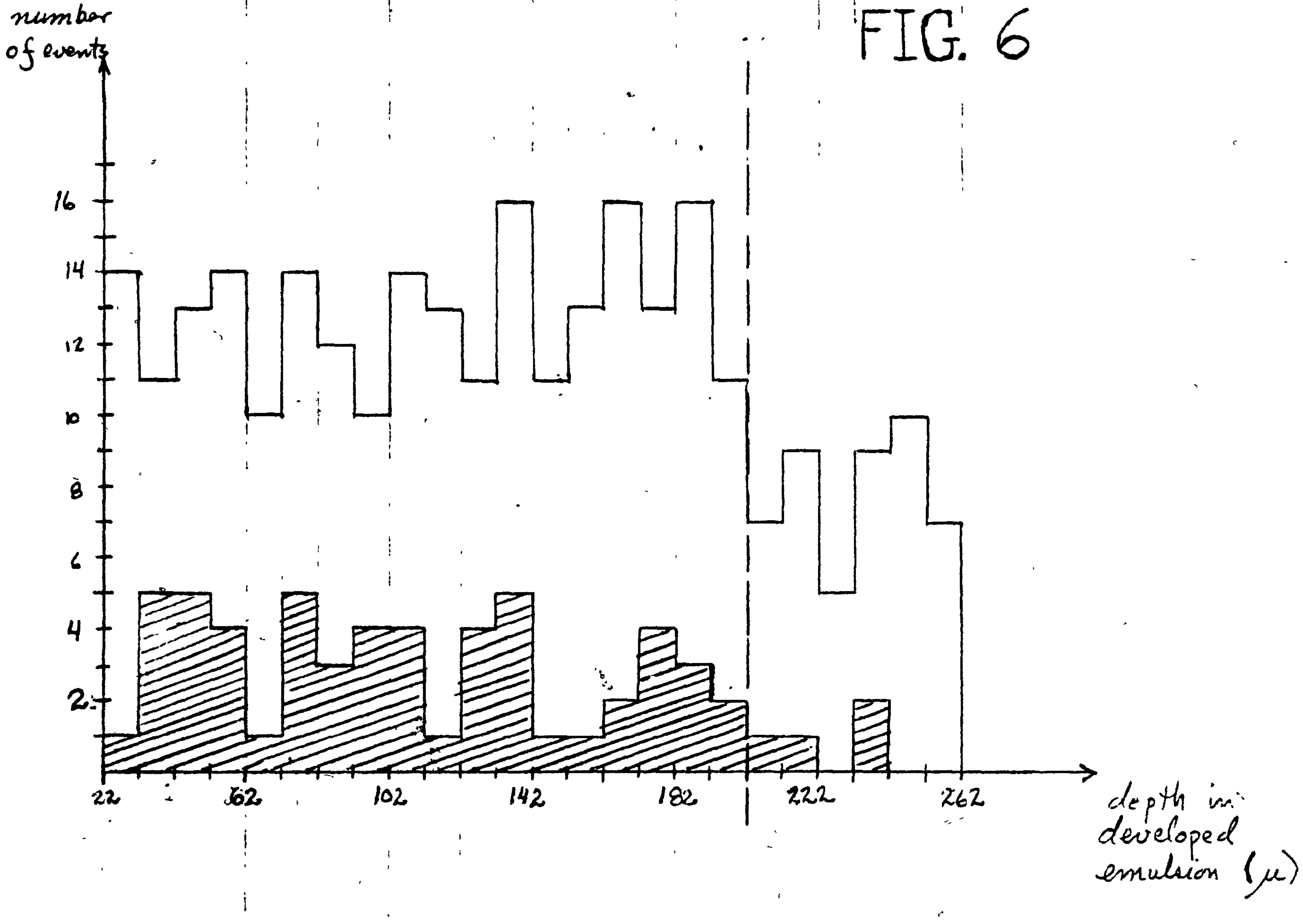
number of events
16
14
12
10
8
6
4
2
22
62
102
142
182
222
262
depth in developed emulsion (μ)

FIG. 7

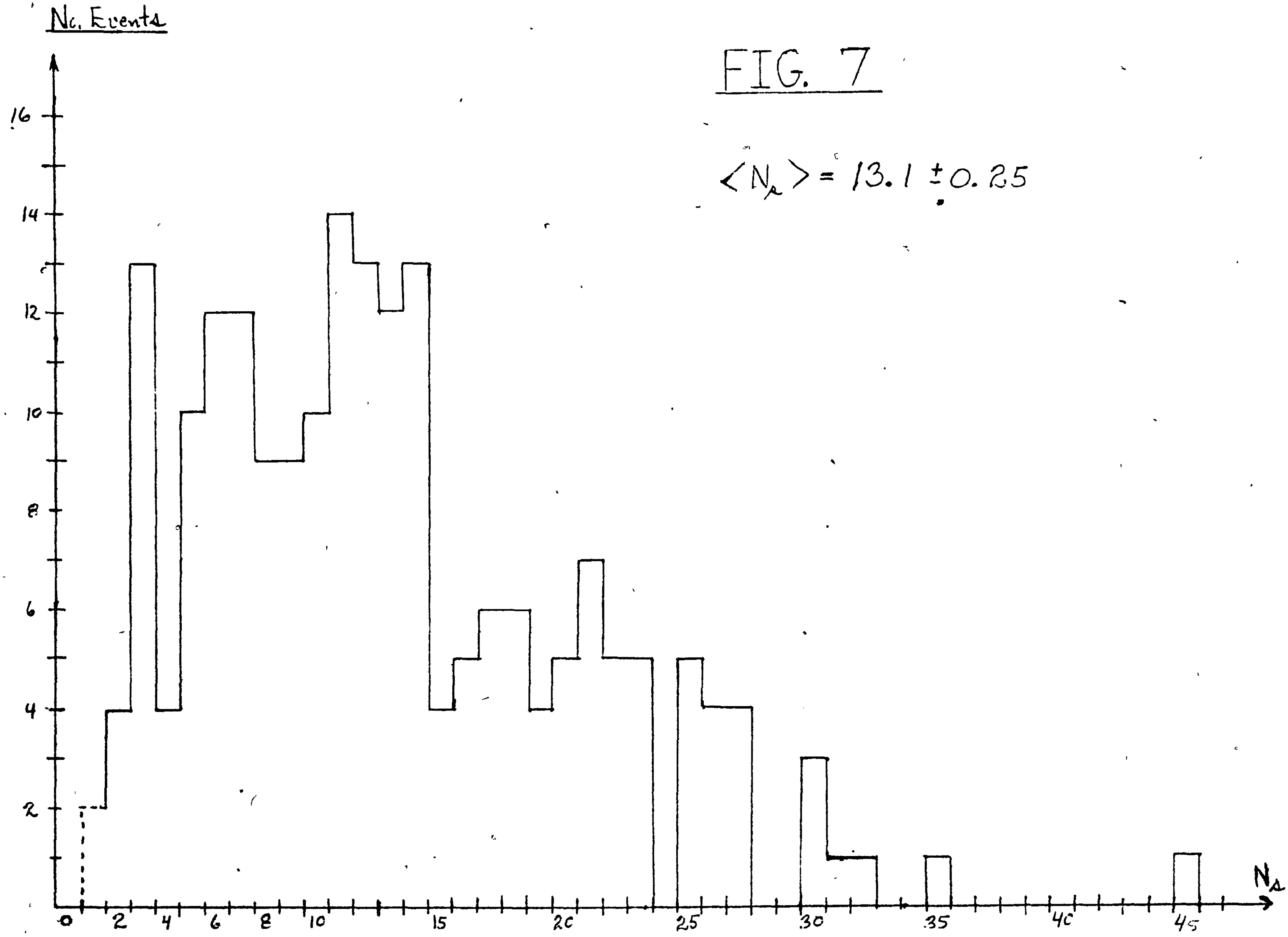

$\langle N_\ell \rangle = 13.1 \pm 0.25$

FIG. 8 Small Stars

$\langle N_s \rangle = 7.4 \pm 0.4$

$\langle N_s \rangle_{even} = 7.8 \pm 0.6$

$\langle N_s \rangle_{odd} = 7.0 \pm 0.5$

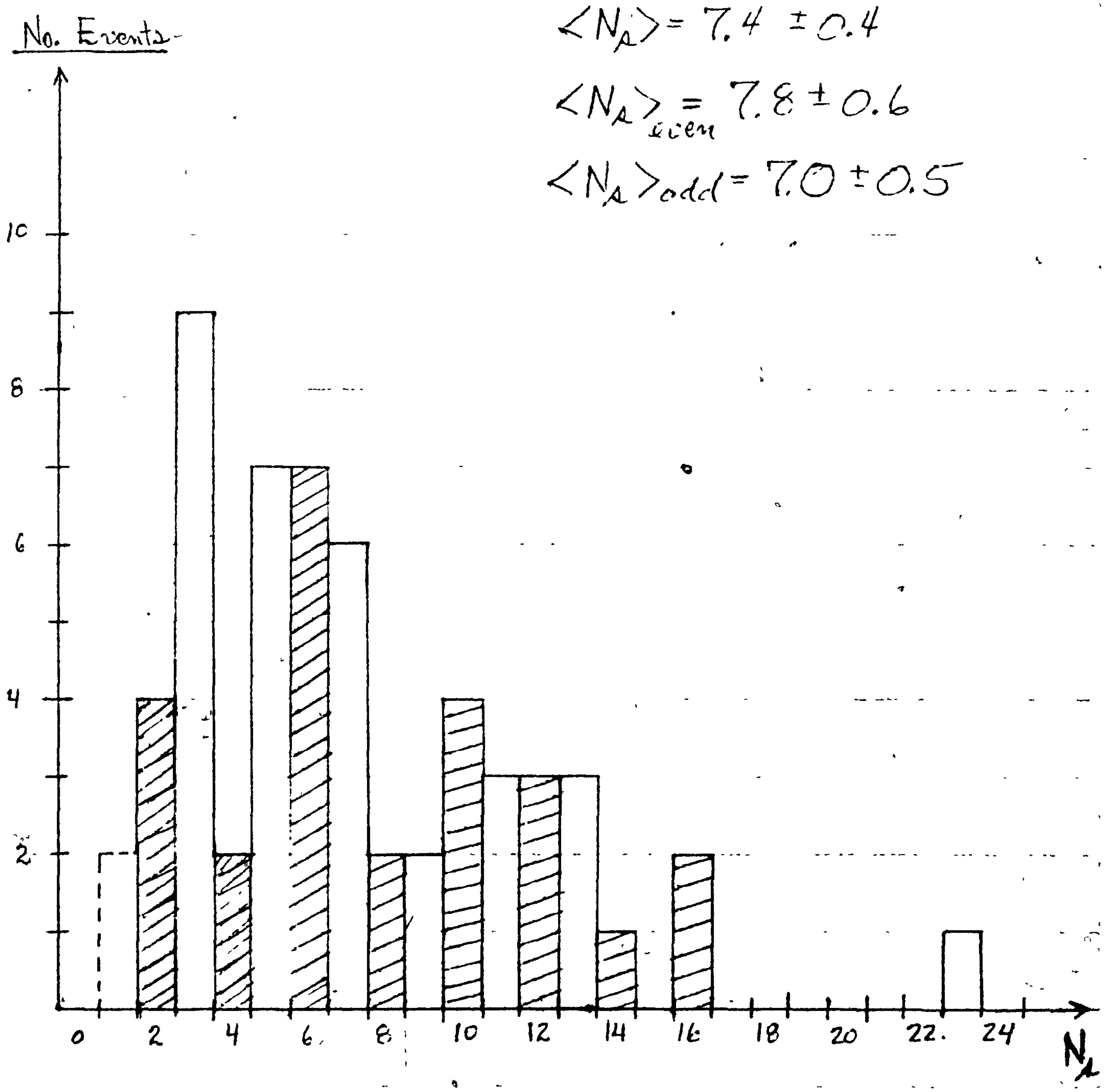

FIG. 9

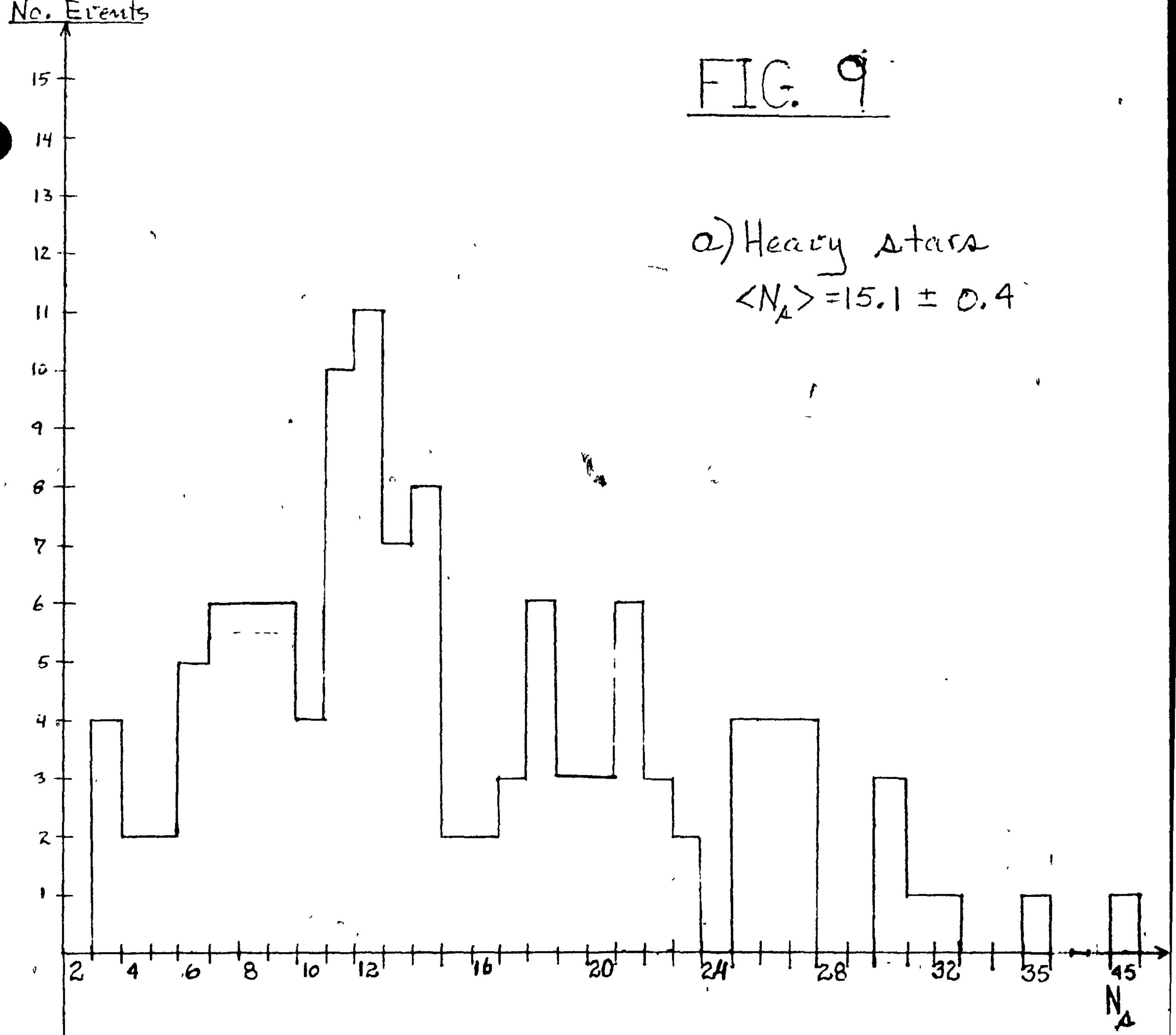

a) Heavy stars
$\langle N_s \rangle = 15.1 \pm 0.4$

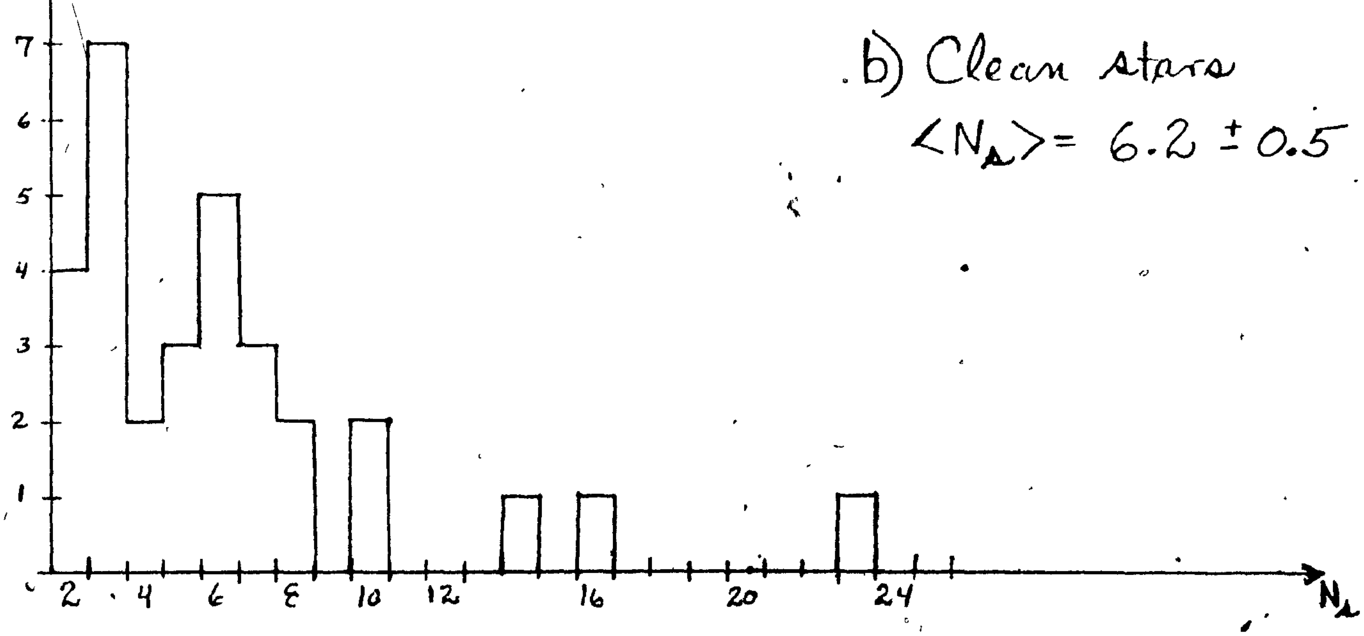

b) Clean stars
$\langle N_s \rangle = 6.2 \pm 0.5$

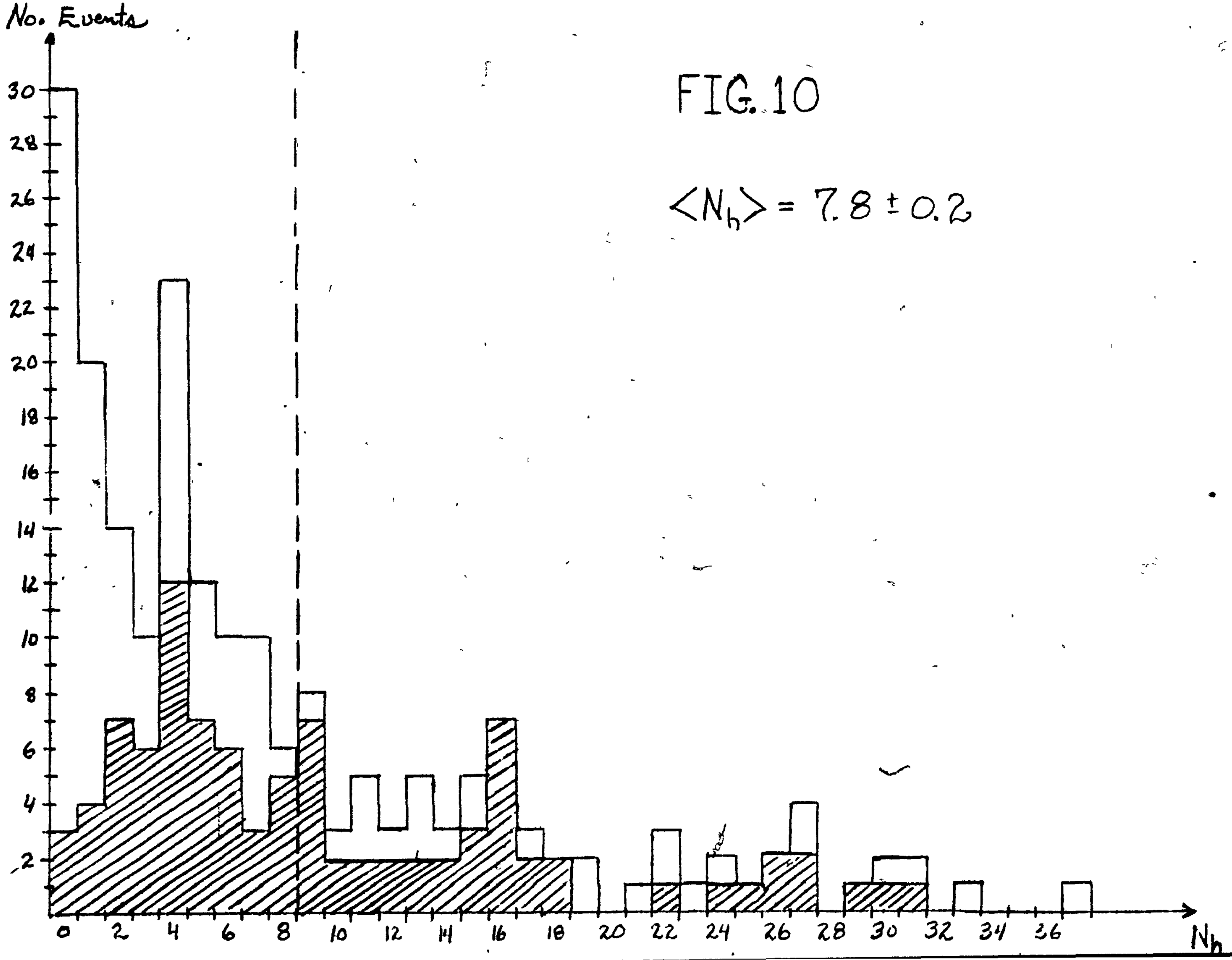

FIG. 10

$\langle N_h \rangle = 7.8 \pm 0.2$

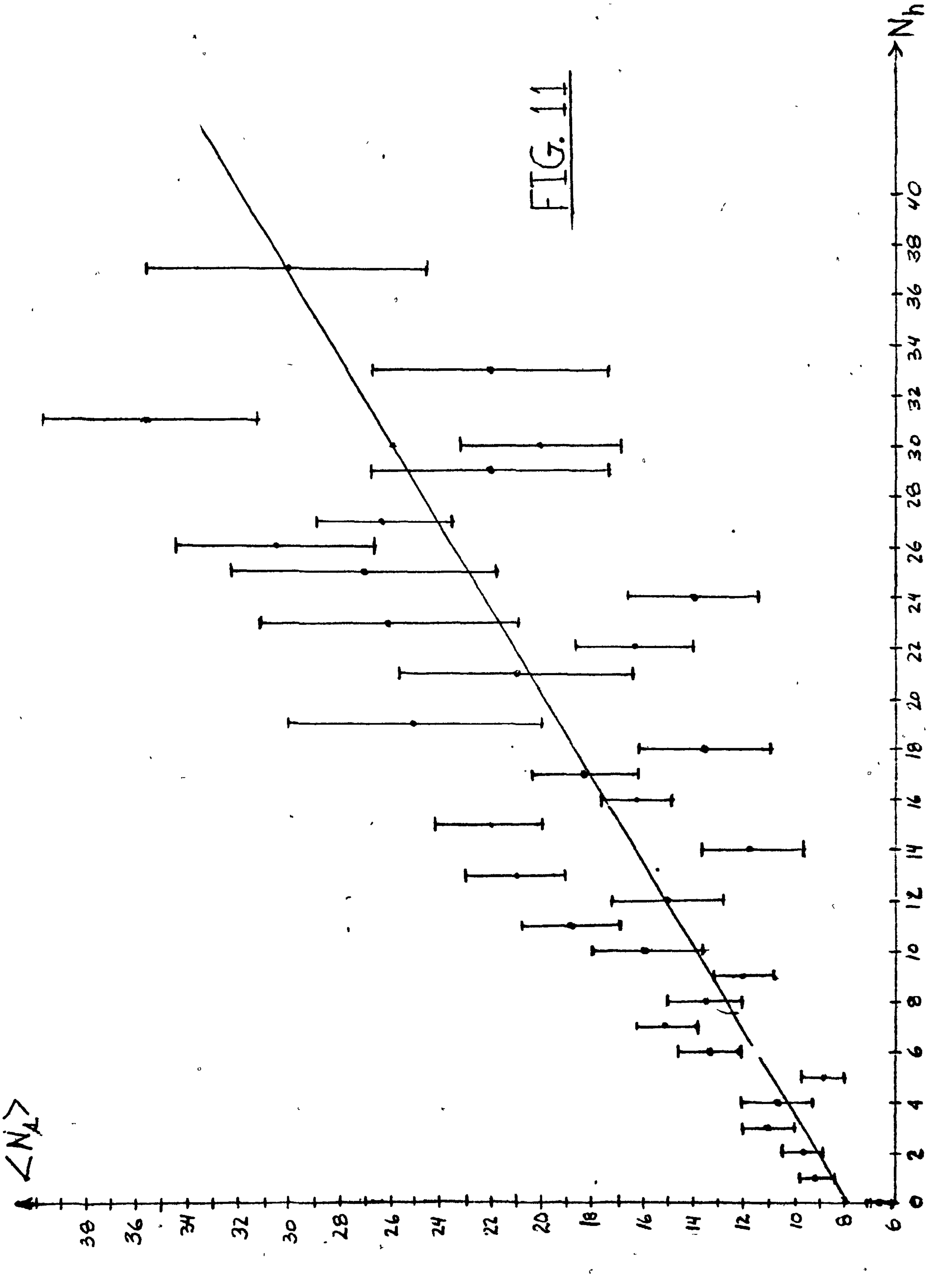

$\langle N_\perp \rangle$
N_h
0
2
4
6
8
10
12
14
16
18
20
22
24
26
28
30
32
34
36
38
40
6
8
10
12
14
16
18
20
22
24
26
28
30
32
34
36
38

FIG. 11

FIG. 12

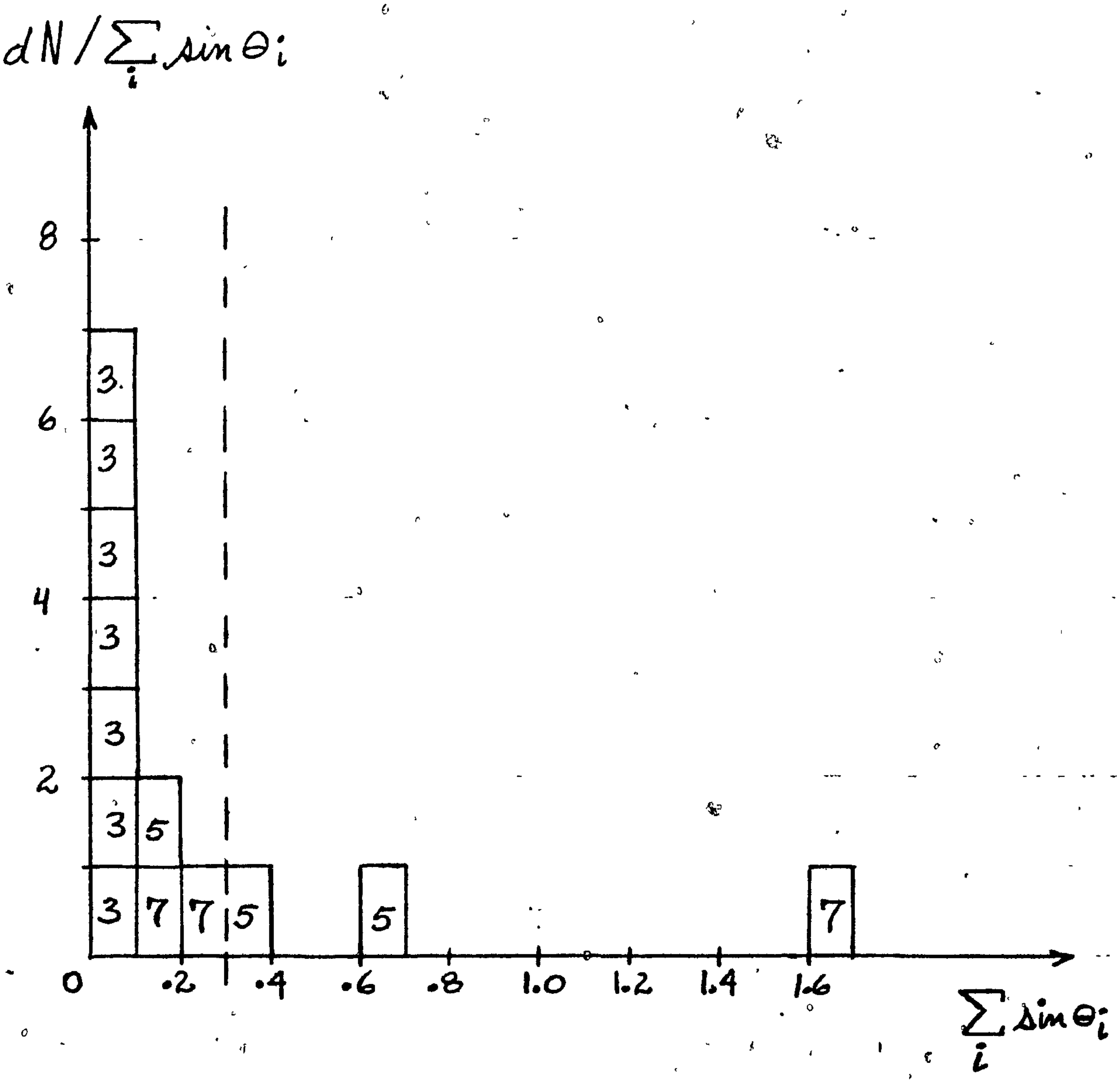

$dN/\sum_i \sin\theta_i$
8
6
4
2
0
3
3
3
3
3
3
3
5
7
7
5
5
7
.2
.4
.6
.8
1.0
1.2
1.4
1.6
$\sum_i \sin\theta_i$

FIG. 13

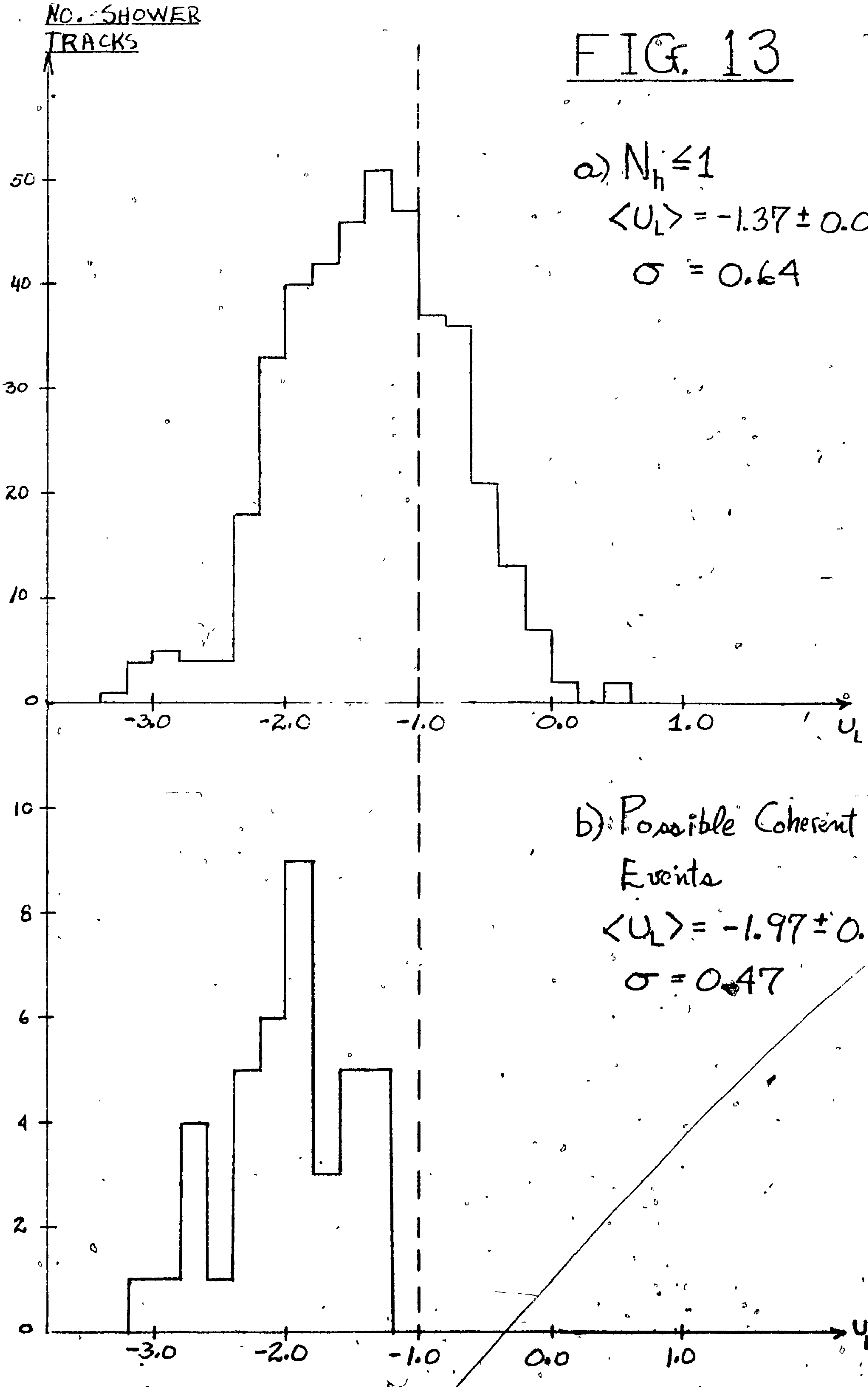

a) $N_h \leq 1$

$\langle U_L \rangle = -1.37 \pm 0.06$

$\sigma = 0.64$

b) Possible Coherent Events

$\langle U_L \rangle = -1.97 \pm 0.22$

$\sigma = 0.47$

FIG. 14

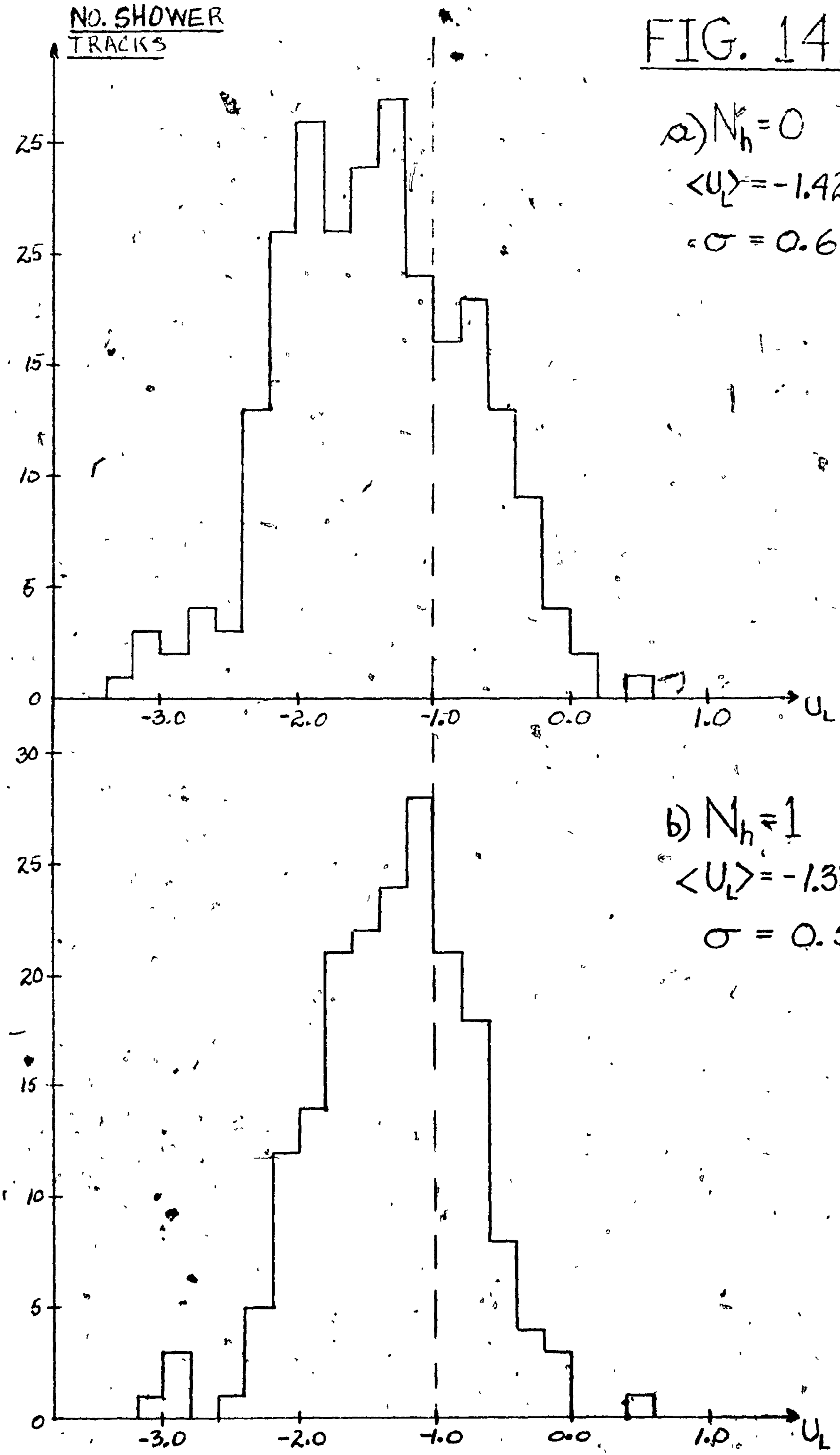

a) $N_h = 0$

$\langle U_L \rangle = -1.42 \pm 0.08$

$\sigma = 0.68$

b) $N_h = 1$

$\langle U_L \rangle = -1.32 \pm 0.08$

$\sigma = 0.58$

FIG. 15

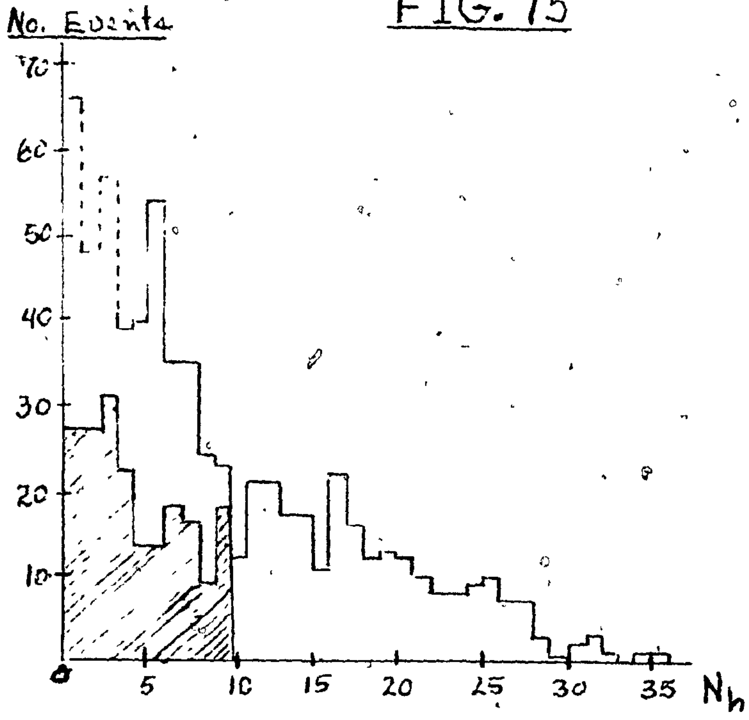
No. Events
70
60
50
40
30
20
10
0
5
10
15
20
25
30
35
N_h

FIG. 16

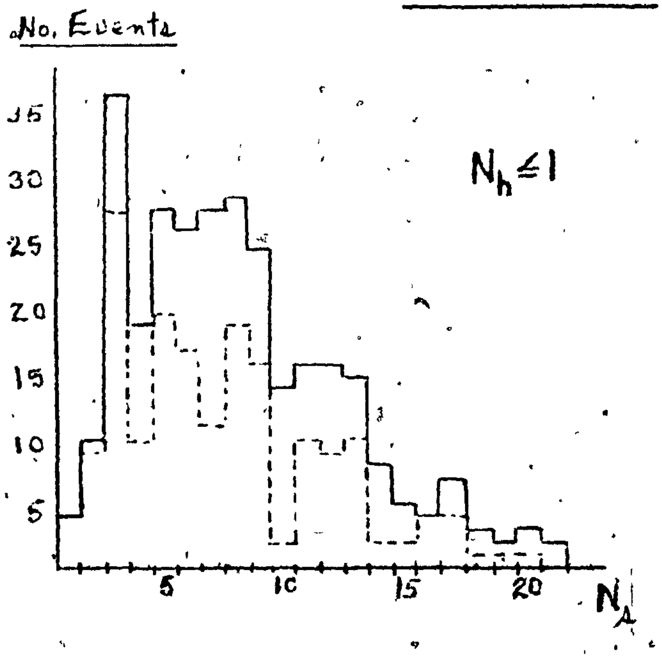
No. Events
35
30
25
20
15
10
5
$N_h \leq 1$
5
10
15
20
N_A

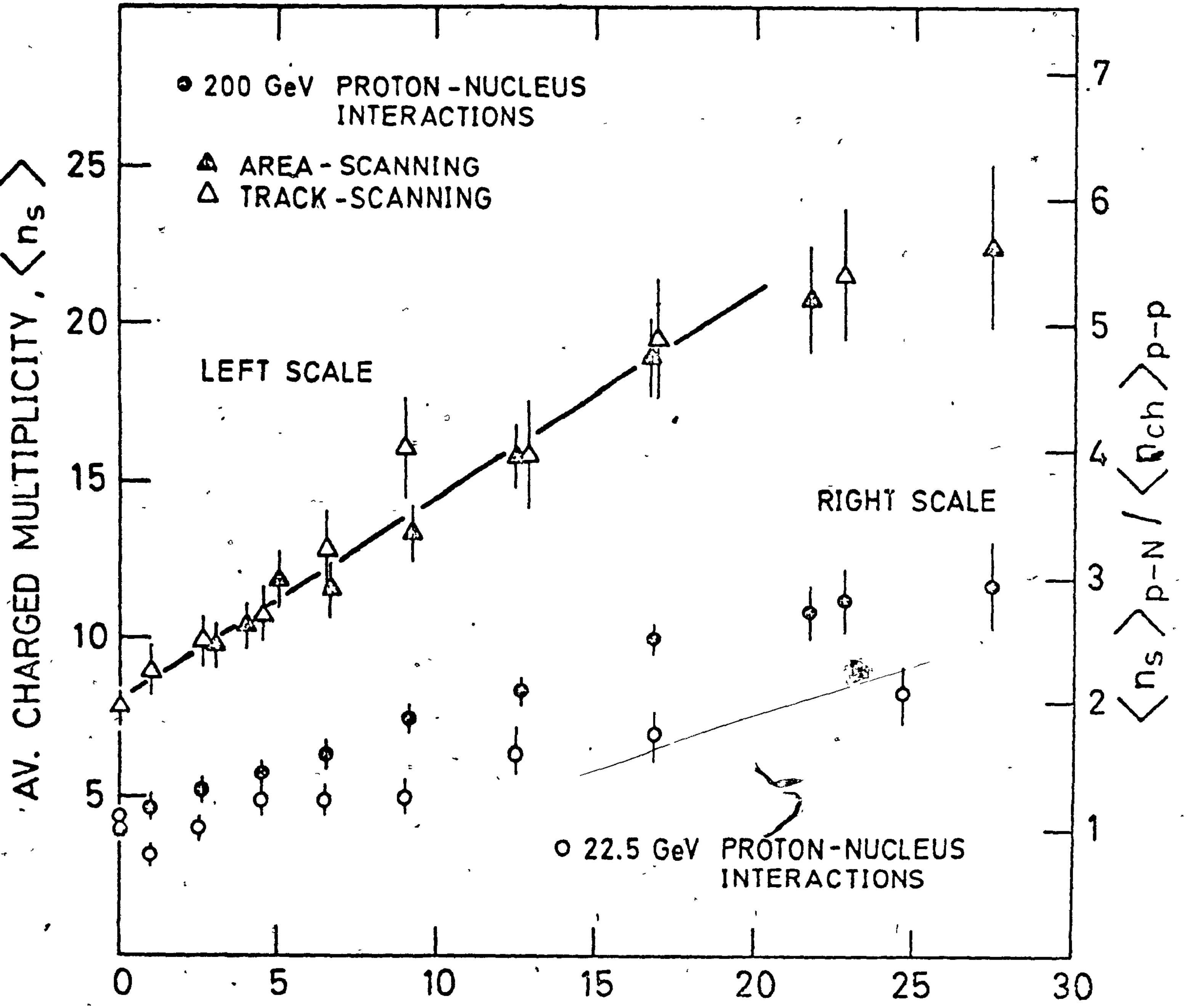

200 GeV PROTON-NUCLEUS INTERACTIONS
AREA-SCANNING
TRACK-SCANNING
LEFT SCALE
RIGHT SCALE
22.5 GeV PROTON-NUCLEUS INTERACTIONS
AV. CHARGED MULTIPLICITY, $\langle n_s \rangle$
$\langle n_s \rangle_{p-N} / \langle n_{ch} \rangle_{p-p}$
NUMBER OF HEAVY PRONGS, N_h
0
5
10
15
20
25
30
1
2
3
4
5
6
.7

FIG. 17

FIG. 18

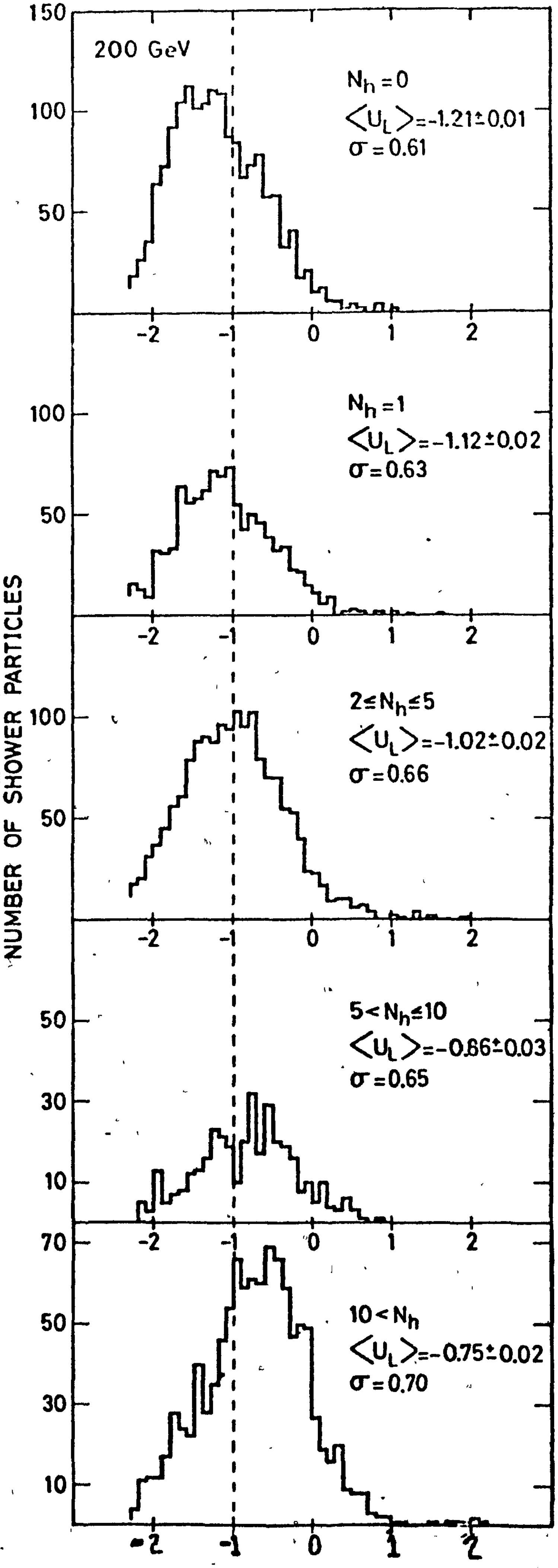
200 GeV
NUMBER OF SHOWER PARTICLES
$N_h = 0$
$\langle U_L \rangle = -1.21 \pm 0.01$
$\sigma = 0.61$
$N_h = 1$
$\langle U_L \rangle = -1.12 \pm 0.02$
$\sigma = 0.63$
$2 \leq N_h \leq 5$
$\langle U_L \rangle = -1.02 \pm 0.02$
$\sigma = 0.66$
$5 < N_h \leq 10$
$\langle U_L \rangle = -0.86 \pm 0.03$
$\sigma = 0.65$
$10 < N_h$
$\langle U_L \rangle = -0.75 \pm 0.02$
$\sigma = 0.70$
150
100
50
100
50
100
50
50
30
10
70
50
30
10
-2
-1
0
1
2

FIG. 19

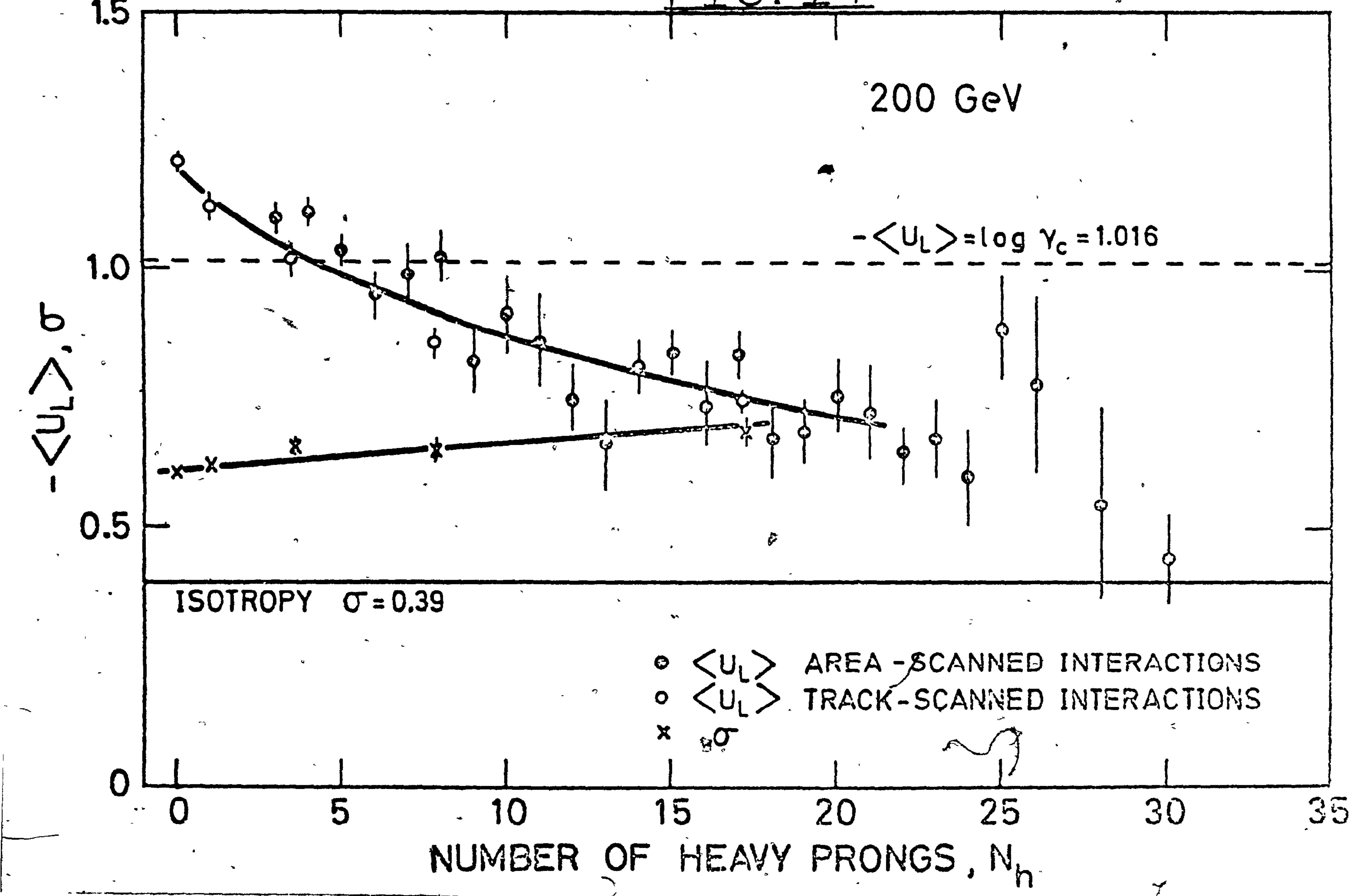

200 GeV
$-\langle U_L \rangle = \log \gamma_c = 1.016$
ISOTROPY $\sigma = 0.39$
$\langle U_L \rangle$ AREA-SCANNED INTERACTIONS
$\langle U_L \rangle$ TRACK-SCANNED INTERACTIONS
x σ
$-\langle U_L \rangle, \sigma$
1.5
1.0
0.5
0
0
5
10
15
20
25
30
35
NUMBER OF HEAVY PRONGS, N_h

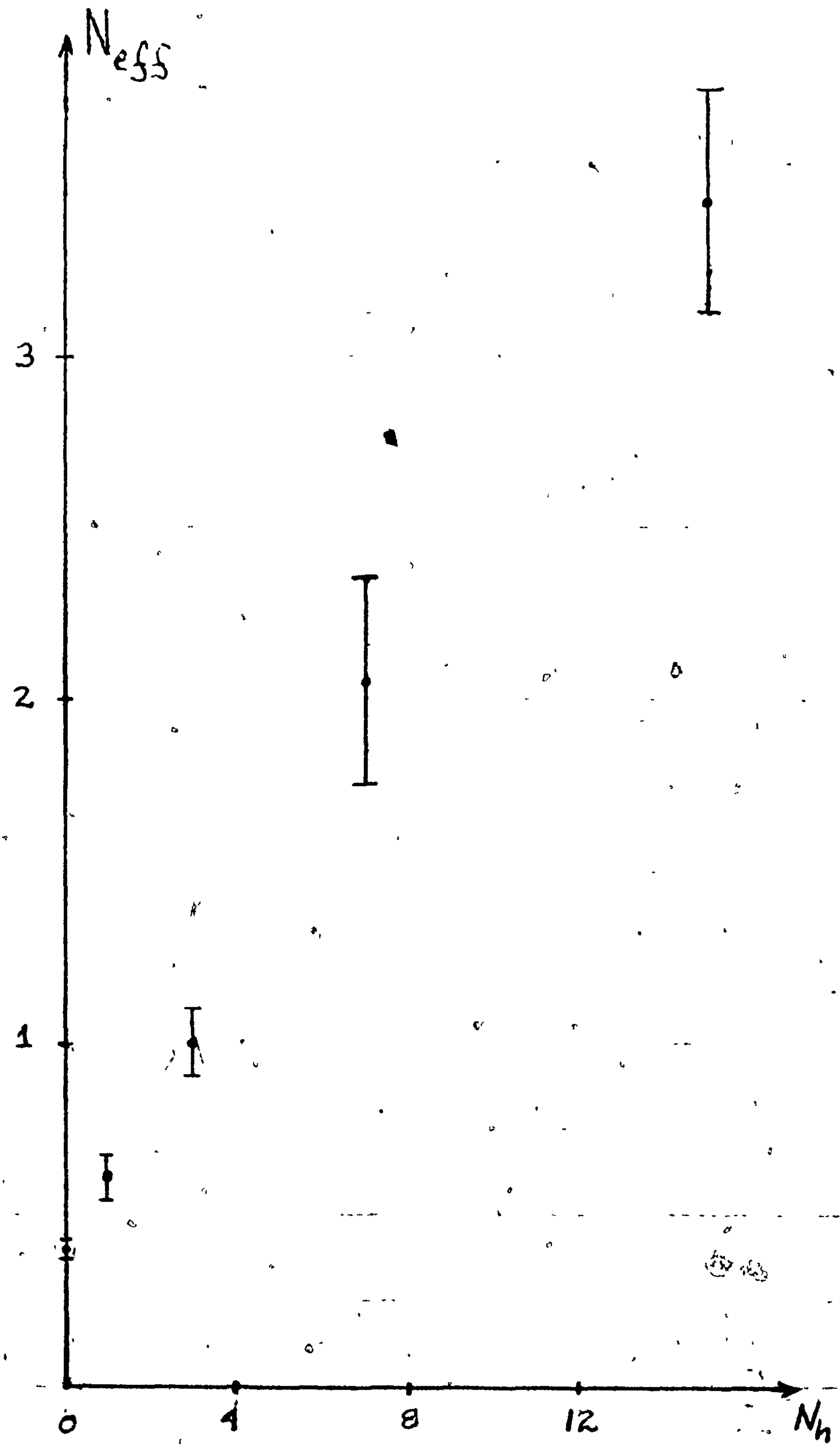

FIG. 20

FIG. 21

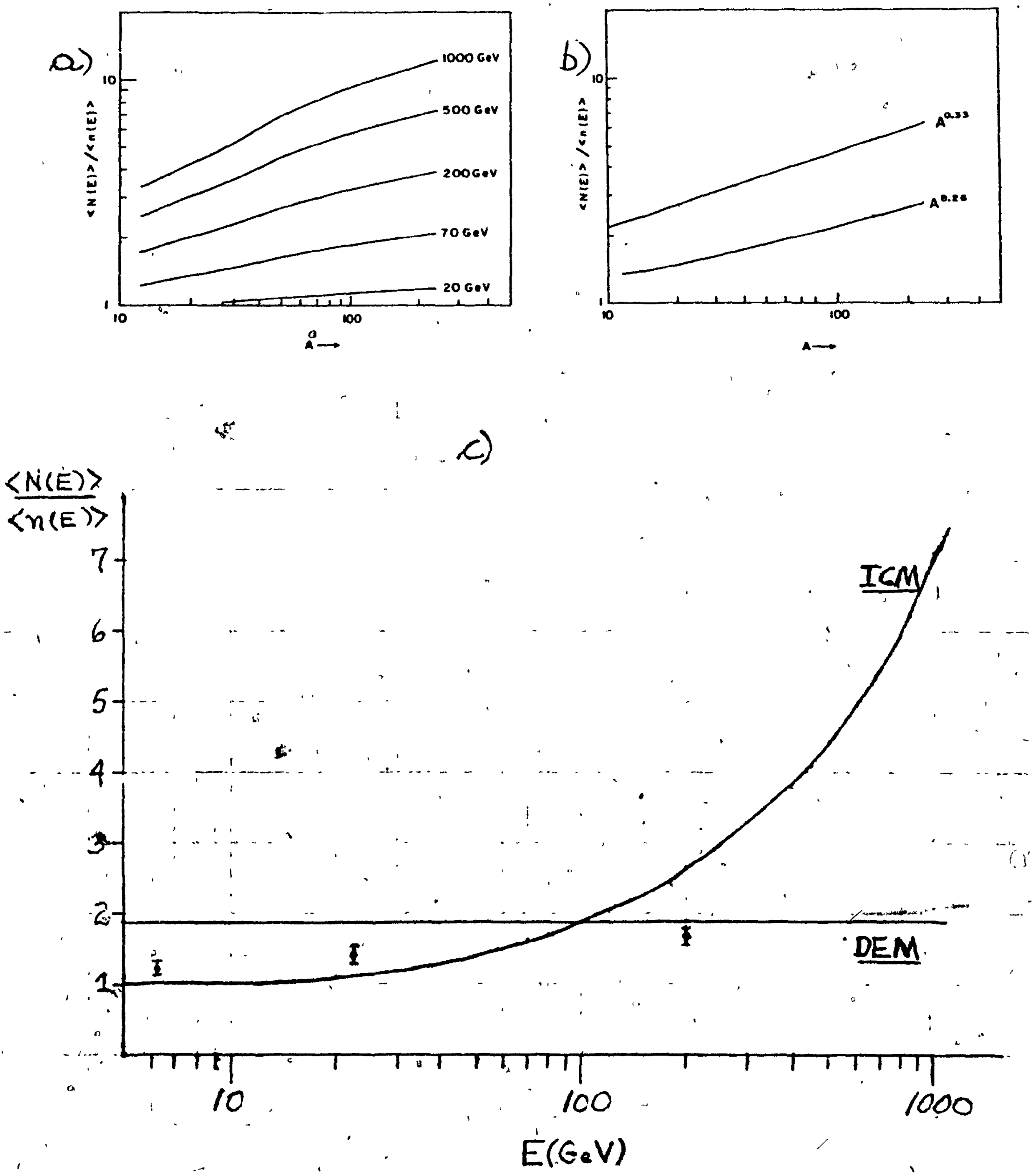

a)
<N(E)>/<n(E)>
10
1
10
100
A⟶
1000 GeV
500 GeV
200 GeV
70 GeV
20 GeV
b)
<N(E)>/<n(E)>
10
1
10
100
A⟶
$A^{0.33}$
$A^{0.26}$
c)
<N(E)>/<n(E)>
7
6
5
4
3
2
1
ICM
DEM
10
100
1000
E(GeV)

FIG 22

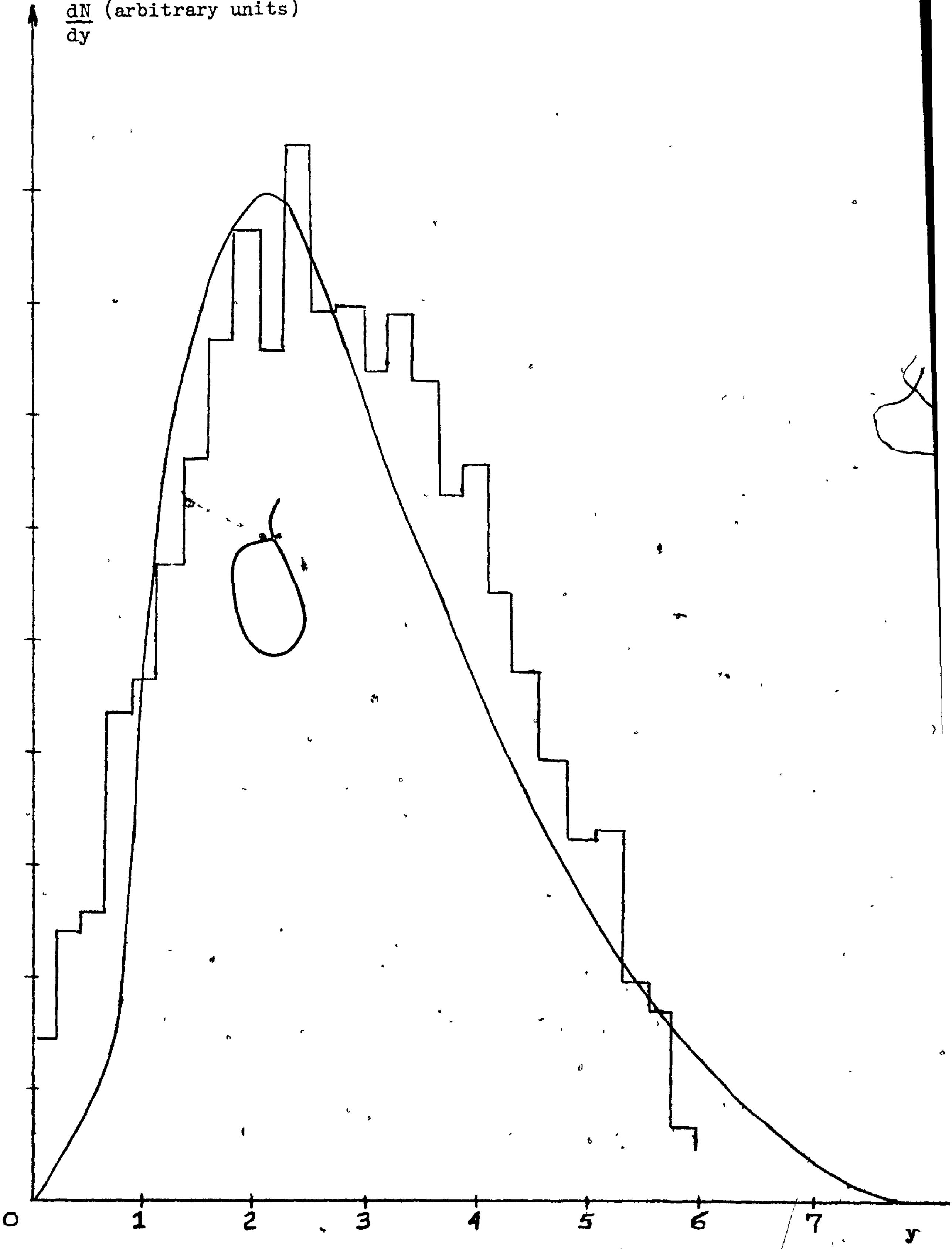

FIG. 23

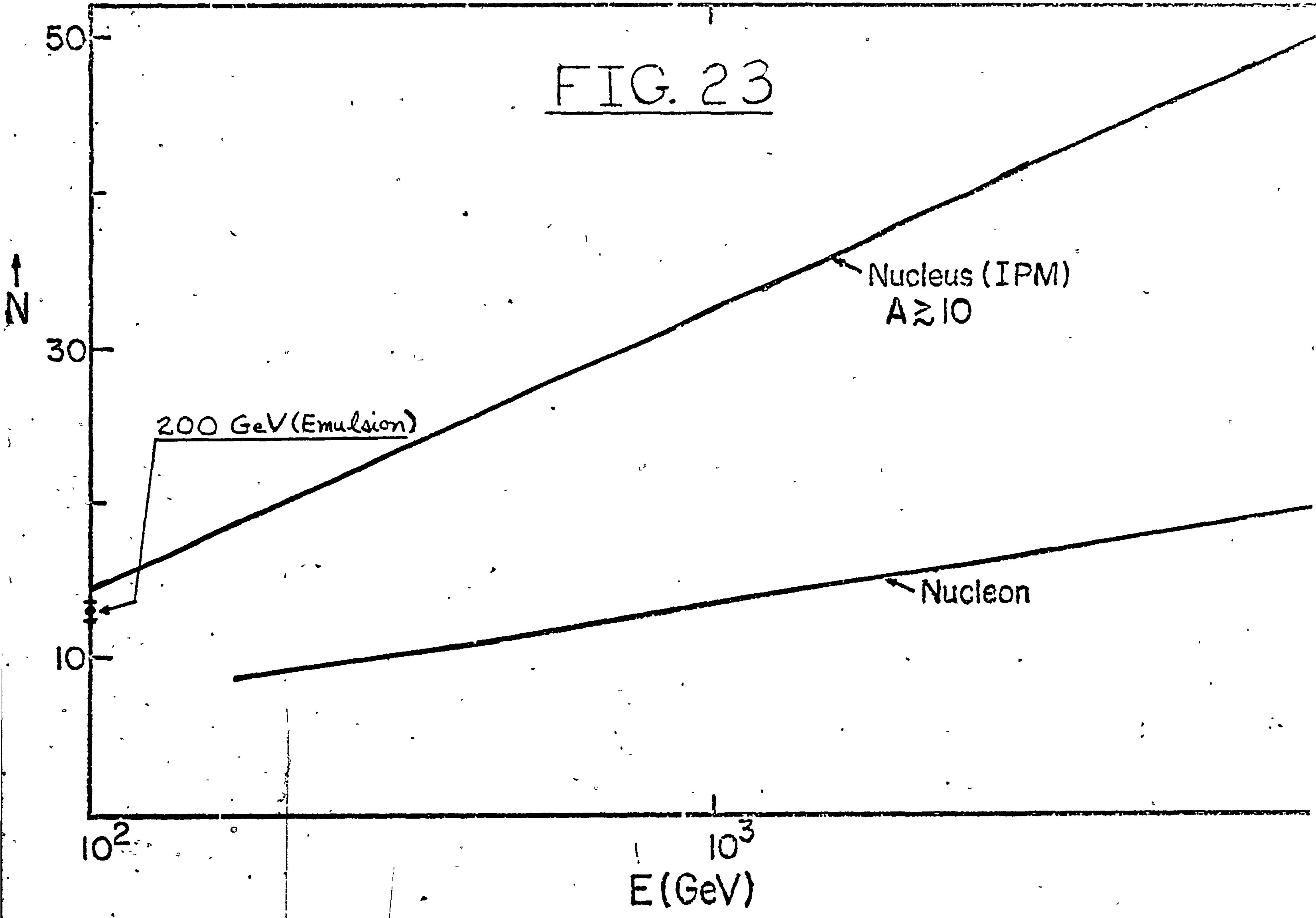

50
30
10
N
200 GeV (Emulsion)
Nucleus (IPM)
A ≳ 10
Nucleon
10^2
10^3
E (GeV)